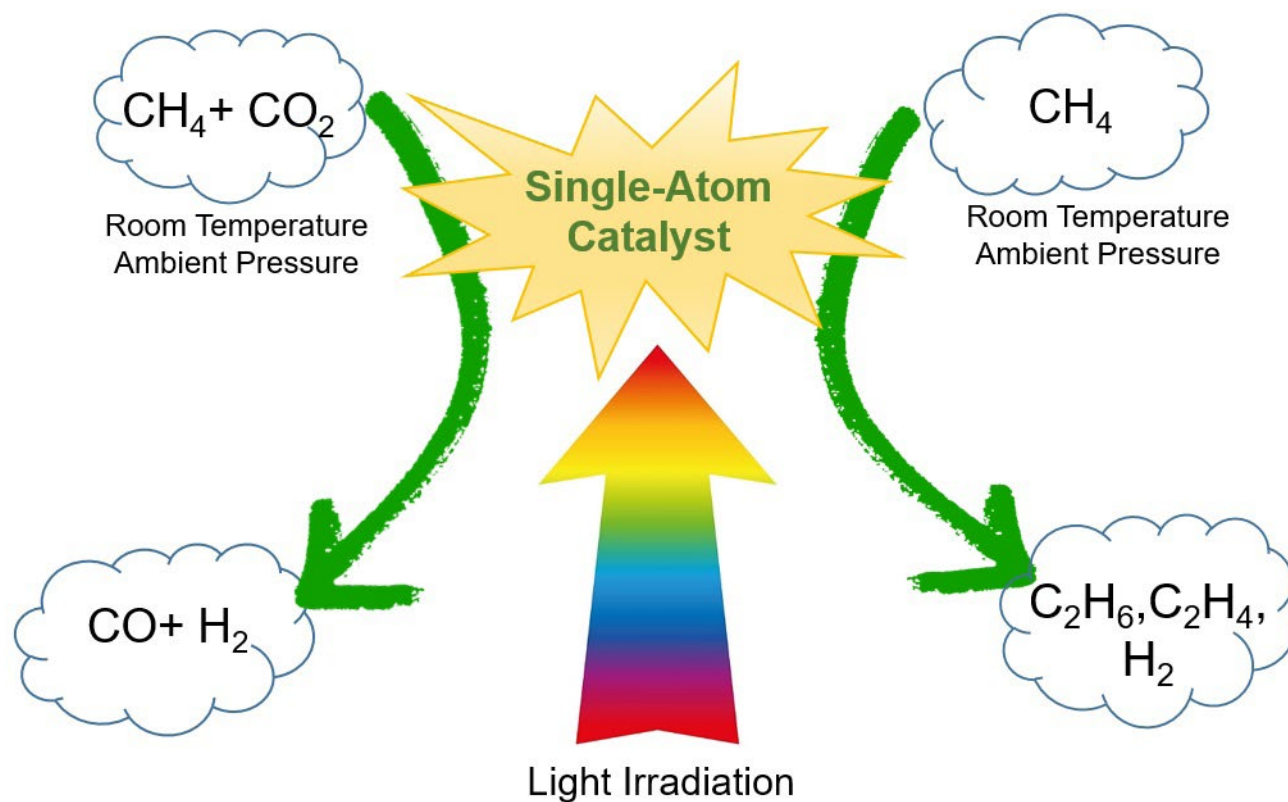


# GRAPHICAL ABSTRACT



# Low-Temperature Methane Conversion over Single-Atom Photocatalysts (a Review)

N. N. Ezhova<sup>a,\*</sup>, K. B. Golubev<sup>a</sup>, Yu. M. Snatenkova<sup>a</sup>, and N. V. Kolesnichenko<sup>a,\*\*</sup>

<sup>a</sup> Topchiev Institute of Petrochemical Synthesis, Russian Academy of Sciences, Moscow, 119991 Russia

\*e-mail: ezhova@ips.ac.ru; \*\*e-mail: nvk@ips.ac.ru

Received June 21, 2024; revised March 13, 2025; accepted March 18, 2025

**Abstract**—Single-atom catalysts (SACs) are the latest generation of nanoheterogeneous catalysts. They consist of active metal sites dispersed into single atoms on the surface of a solid support and, thus, exhibit unique catalytic performance including enhanced activity and high selectivity. Semiconductor materials are used to prepare single-atom photocatalysts designed for photo-driven chemical processes, generally without external heating. Photoinduced low-temperature methane conversion over SAC-based photocatalysts offers new prospects for methane chemistry. This review summarizes, systematizes, and analyzes recent publications on dry reforming of methane (DRM) and nonoxidative coupling of methane (NOCM) in the presence of single-atom photocatalysts. Despite the unfavorable thermodynamics of these types of reactions over wide ranges of low and high temperatures, they can be carried out at room temperature under photocatalytic conditions. The review discusses the performance of SACs in photoinduced DRM and NOCM compared to heterogeneous nanocatalysts. It further provides a comparative assessment of the SAC behaviors in DRM and NOCM under photocatalytic and conventional thermocatalytic conditions.

**Keywords:** photocatalysis, single-atom catalysts, low-temperature methane conversion, nonoxidative coupling of methane, dry reforming of methane

**DOI:** 10.1134/S096554412560047X

As the principal component of natural gas, methane is currently one of the major fossil fuels. The application of this carbonaceous raw material instead of conventional petroleum feedstocks has become an advantageous strategy for the industrial synthesis of value-added chemicals. Today, methane-based chemical synthesis is of great importance both for the Russian market—the world leader in natural gas reserves and production—and for countries that increasingly produce shale gas and, consequently, face the challenge of the disposal of methane as a greenhouse gas [1, 2].

However, the thermal stability of the CH<sub>4</sub> molecule impedes the implementation of methane-based synthesis: high amounts of energy are required to activate the strong C–H bonds. Therefore, only high-temperature thermocatalytic techniques are currently used for industrial methane processing. In facilities of this kind, methane is converted—primarily through synthesis gas (syngas)—into methanol, formaldehyde, acetic acid, ethylene, hydrogen, polymers, and other petrochemicals

[3, 4]. Nonetheless, recent chemical research has increasingly focused on the development of alternative low-temperature methods for the conversion of methane into these value-added chemicals [5–8], including a combination of catalysis with exposure to various high-energy fields (e.g., low-temperature plasma [8–10], electrical energy [6, 11, 12], and photon energy [11, 13–17]). Although all these methods hold great promise for the activation of inert chemical bonds under low-temperature conditions [7, 17, 18], photocatalysis is a unique technique that reduces the energy barrier of the C–H bond in the CH<sub>4</sub> molecule by at least 74% [19]. This offers an opportunity to carry out methane reactions even at room temperature and, moreover, provides a fairly high selectivity towards the desired product [6]. Researchers have particular expectations for the photocatalytic application of highly dispersed single-atom catalysts (SACs) [20–25], an innovative approach to methane chemistry [20, 26].

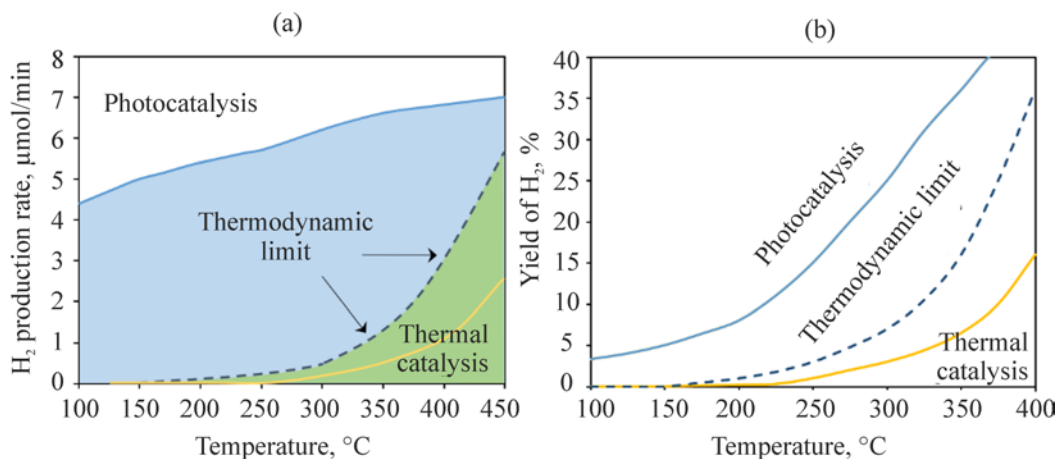


**Fig. 1.** Overcoming the thermodynamic limit in DRM when transitioning from thermal catalysis to photocatalysis: (a) Rh/SrO<sub>3</sub> under UV irradiation (reproduced from [31]); and (b) Rh/TaON under visible light irradiation (at  $\lambda \geq 400$  nm) (reproduced from [46]).

SACs with isolated metal atoms on the surface of a solid support have proven to be highly active and selective catalysts in a number of thermocatalytic applications [5, 27–29], including those that involve CH<sub>4</sub> [5, 30]. According to available forecasts, photocatalytic methane activation over these highly dispersed catalysts will make it possible to directly convert CH<sub>4</sub> to C<sub>1</sub>–C<sub>2</sub> hydrocarbons under light irradiation and achieve high efficiency minimal energy consumption [20, 26].

The purpose of the present review was to demonstrate the excellent prospects of this innovative approach for chemical reactions with unfavorable thermodynamics, such as dry reforming of methane (DRM) [31] and nonoxidative coupling of methane to C<sub>2</sub> hydrocarbons (NOCM) [32].

#### PHOTOCATALYSIS IN METHANE CHEMISTRY

Of particular interest are photochemical transformations of CH<sub>4</sub> under artificial light irradiation (e.g., light-emitting diodes, xenon lamps, and other unconventional illumination sources) [13–18, 33–37]. In this context, the use of focused illumination has recently attracted increasing attention among researchers [38–45].

This approach gained in popularity after thermodynamic limitations were overcome for some direct CH<sub>4</sub> conversion reactions [31, 46], such as NOCM [32] and DRM [38]. When photo-driven, these reactions occur at moderate and low temperatures regardless of light frequency or catalyst

type (Fig. 1). Under photocatalytic conditions, the system goes beyond the thermodynamic equilibrium limit due to the transformation of photon energy into chemical driving forces. Specifically, photoexcited charge carriers such as electrons (e<sup>-</sup>) and positively charged electron vacancies (the so-called “holes”, h<sup>+</sup>) are involved in the process by initiating reduction and oxidation reactions, respectively [17, 38]. The C–H bonds of CH<sub>4</sub> can undergo oxidative dissociation either directly on the semiconductor holes or under the effect of mediators (e.g., ·OH, O<sup>-</sup>, etc.) that form on the photogenerated holes if oxidants (H<sub>2</sub>O<sub>2</sub>, O<sub>2</sub>, CO<sub>2</sub>, and/or H<sub>2</sub>O) are involved in methane conversion [17, 38]. In their turn, the photogenerated electrons promote the reduction process ( $H^+ + e^- \rightarrow 1/2 H_2$ ).

Any photocatalytic reaction consists of three major steps: (i) absorption of light quanta ( $h\nu$ ); (ii) generation and spatial separation of charges (e<sup>-</sup> and h<sup>+</sup>); and (iii) the catalytic reaction itself. The overall efficiency of a photocatalytic system is determined by the balance between the thermodynamics and kinetics of these reaction steps [15, 38]. The catalytic performance of a semiconductor material entirely depends on the ability of its components to catalyze, on its surface, a particular chemical reaction. In contrast, the quantum efficiency of a photocatalytic system depends both on the light absorbance by the photocatalyst and on the separation efficiency of electron–hole pairs [38]. In order to ensure the separation of electrons and holes, the semiconductor should be able to absorb a light quantum ( $h\nu$ ) that exceeds

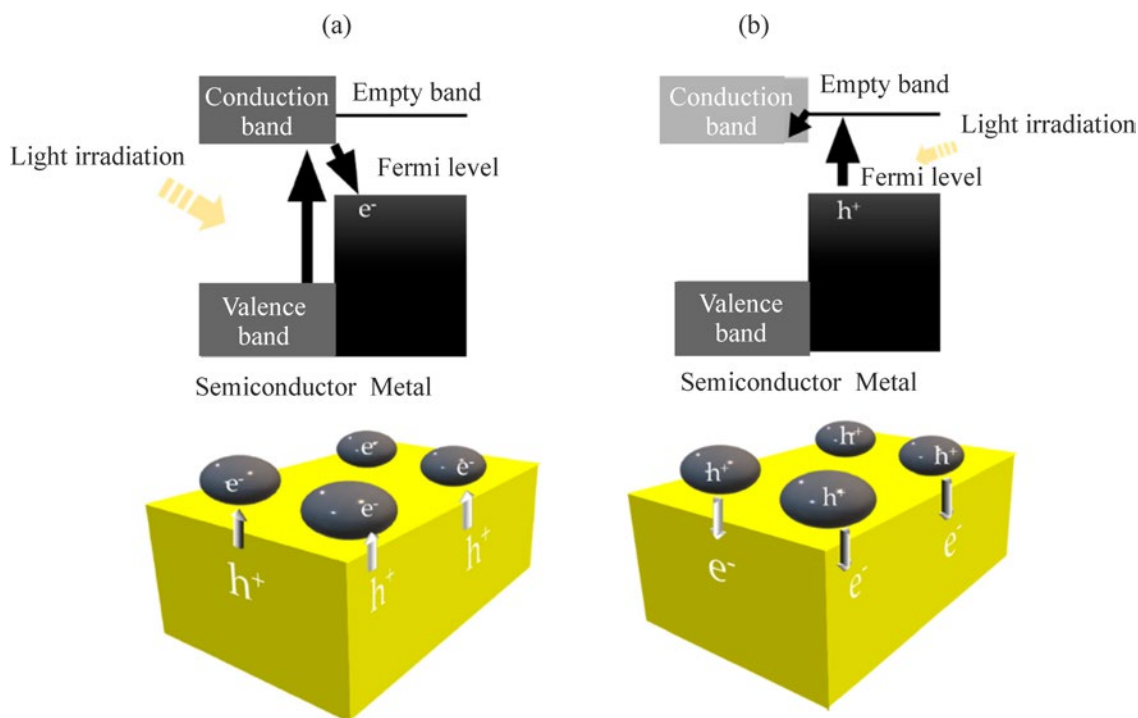


**Fig. 2.** Photoexcitation mechanisms for  $e^-$  and  $h^+$  under light irradiation of metal-doped semiconductor catalysts: (a) electron transfer pathway from conduction band to Fermi level; and (b) excited carriers' pathway in the hot carrier mechanism (electron transfer from Fermi level to conduction band) (reproduced from [2]).

its bandgap energy ( $E_g$ ) (the bandgap is the difference between the energy levels of the conduction band and the valence band, which hold  $e^-$  and  $h^+$ , respectively). Therefore, the quantum efficiency of the photosystem can be enhanced by reducing the photocatalyst's bandgap width and increasing the stability of its photoexcited charges. The various strategies proposed to address this challenge through the improvement of photocatalyst design [15, 47] include, in particular, controlling the semiconductor morphology [14, 48], facet-engineering techniques [49], and introducing defects on the heterogeneous photocatalyst surface [50]. The spatial separation of carriers ( $e^-$  and  $h^+$ ) can be ensured by generating structures with interfacial heterojunctions for photoexcited charges. For this purpose, a number of engineering solutions have been proposed, such as adding electron traps ( $Ag^+$ ,  $Cu^{2+}$ ,  $Fe^{3+}$ ) to a photosystem [14, 51], doping a semiconductor with heteroatoms, and fabricating composite semiconductors [14]. However, the most common approach involves decorating a conventional semiconductor (e.g.,  $TiO_2$  or  $ZnO$ ) with a cocatalyst, usually a noble metal ( $Au$ ,  $Pt$ ,  $Pd$ ,  $Rh$ , etc.) [52]. Small amounts of this cocatalyst (0.1–1.5 wt %) are added to achieve high dispersion of its nanoparticles [53, 54] or

even isolated atoms [21] on the semiconductor surface. The addition of a metal cocatalyst to a semiconductor not only enhances the carrier separation efficiency and the light absorbance but also generates additional active sites (specifically, the atoms and ions of the metal dopants), which facilitate redox reactions by decreasing the reactant activation energies [11, 52]. As a result, metal doping of a photocatalyst accelerates a photocatalytic reaction by a factor of at least 5–10 [55].

Metal doping of a semiconductor can create intraband states below its conduction band (Fig. 2a). Given that a metal's Fermi level is generally located below the bottom of a semiconductor's conduction band, the photogenerated electrons “fall” from the conduction band onto metal particles [2, 38]. As a result, the bandgap of the photocatalytic system is narrowed, and the light absorbance rises, thus markedly enhancing the quantum efficiency. In addition to bandgap excitation, another mechanism has been reported for excitation in combined metal–semiconductor materials (hot carrier mechanism, Fig. 2b). In this case, hot carriers are generated when photons are irradiated onto metal, causing the excitation

of electrons in unoccupied bands, followed by the electron transfer to the semiconductor's conduction band [2, 38].

Hot electrons are known to be generated in highly dispersed photosensitive metal particles (Au, Ag, Cu, Rh, Pd, Ru, etc.) [56]. The photogenerated free electrons in metal nanoparticles can be oscillated collectively under light irradiation through the excitation of localized surface plasmon resonance (LSPR), thus abruptly increasing the absorbance. LSPR takes place when the incident frequency matches the natural frequency of free electrons oscillating in metal nanoparticles on a photocatalyst surface [57, 58]. For LSPR of some metals, the light absorption frequencies essentially occur in the visible and near-IR ranges (43% and 52% of the sunlight spectrum, respectively), whereas the UV radiation accounts for only 5%. Therefore, depositing the nanoparticles of these metals on a semiconductor surface photosensitizes this semiconductor and significantly enhances the quantum efficiency of the photocatalytic system under sunlight irradiation [38, 52].

Hot electrons are known to be excited in a metal at a specific wavelength only. Consequently, a combined metal–semiconductor material has a certain wavelength at which both the bandgap and hot electrons are excited simultaneously, as well as a wavelength at which only one of these mechanisms is workable [38]. The bandgap excitation effect can be totally eliminated when the metal is deposited on a non-conductor (e.g., MCM-41 silicate [58]). In any case, however, the presence of a photosensitive metal in a photocatalyst is able to expand the visible absorption range, enhance the electromagnetic field, and simultaneously induce a thermal effect [59]. Photon irradiation may significantly heat the metal-loaded photocatalyst surface [38]. In this context, photochemical processes can be initiated on heated heterogeneous surfaces by two different mechanisms (separately or in combination): by photoinduced hot electrons and by light-excited photons (photothermal effect) [57, 58]. Some researchers deliberately add thermal energy [38]. They report that, under heating, the bandgap narrows and the photocatalytic activity increases, clearly due to the synergy of the light and heat effects on the semiconductor modified with a metal cocatalyst. These efforts have even given rise to a new area of photochemical research, namely photothermal catalysis [58–61].

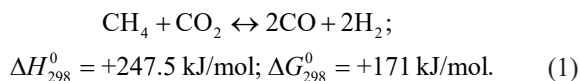
The advantages of photothermal catalysis are most noticeable when the reaction is carried out without external heaters, i.e., when the catalytic surface is heated solely due to the optical properties of the photocatalytic

system [43–46]. Recent research has increasingly taken into account this knowledge to develop novel process designs for low-temperature photoinduced methane conversion in the presence of catalysts with highly dispersed metal dopants [17, 22, 45]. Although these processes are nominally carried out at room temperature, the photocatalyst promotes the transformation of solar energy to thermal energy, thus markedly heating its surface, and the electromagnetic field induced by hot carriers initiates catalysis.

Along with the photocatalyst type, the photon source properties such as the wavelength ( $\lambda$ ) and intensity ( $I$ ) of emitted light are critical to photothermal processes. These properties have a major effect both on the reaction temperature developed on the catalytic surface and on the process performance. Visible light ensures that the methane-activating metal is involved in photocatalysis, whereas IR radiation maintains a high photocatalyst surface temperature, the value of which is largely determined by the light intensity. State-of-the-art optical technology makes it possible to focus the light flux by means of specialized lenses, thus reaching high intensity, equivalent to 30 to 400 suns (or, in terms of  $I$  value, up to 3.6–19.2 W/cm<sup>2</sup>). As a consequence, the photocatalyst surface can be heated to 300–727°C even without an external heater [43–45, 46].

## PHOTOINDUCED DRY REFORMING OF METHANE

Recent years have witnessed the publication of many review papers on DRM (reaction (1)) under photothermal catalytic conditions [2, 17, 62–66], and the amount of research in this area has been steadily growing [39–45, 67–74]. The great interest in photocatalytic conversion of methane and carbon dioxide to syngas is fairly predictable for at least two reasons: (1) this process involves two thermostable molecules [62, 75]; and (2) both are greenhouse gases [2, 75–79].



Under photoirradiation, the endothermic and thermodynamically unfavorable reaction (1) can occur on the photocatalytic surface even without external heating [31, 39, 40, 43–45, 80]. Light radiation acts as a heater and accelerates the dissociation of the C–H bonds of methane, thus notably decreasing the activation energy

of the reaction. In the presence of photocatalysts doped with highly dispersed metals, the rate of this photothermal catalytic reaction can reach 0.4 to 2649 moles of CH<sub>4</sub> per 1 kg of the catalyst per hour (mol kg<sup>-1</sup> h<sup>-1</sup>) [31, 39, 40, 43–45, 80].

Most photocatalytic systems known for reaction (1) contain nanoparticles of a metal cocatalyst such as Rh [31, 81, 82], Pd [80], Ru [43, 44], Pt [41, 42, 83–85], and Ni [39, 40, 69–74]. Recently, the use of a SAC (specifically, Ru<sub>1</sub>@Cu<sub>n</sub>/MgO–Al<sub>2</sub>O<sub>3</sub>) in photocatalytic DRM has been reported for the first time [45]. This system contained a single-atom alloy in which single Ru atoms (activation sites for CH<sub>4</sub> molecules) were surrounded by plasmonic Cu nanoparticles (acting as an antenna) up to 5 nm in size (with resonance at λ = 560 nm). The local optical field induced by the copper antenna effectively converted the catalyst into a photocatalyst [86], and the combination of the plasmonic antenna with single Ru atoms imparted specific properties to the nanostructure. The Ru<sub>1</sub>@Cu<sub>n</sub>/MgO–Al<sub>2</sub>O<sub>3</sub> catalyst stably promoted the reaction under photothermal conditions for at least 50 hours at ambient pressure without external heating. As a result, methane and carbon dioxide were converted beyond the thermodynamic equilibrium with a high rate, 100% hydrogen selectivity (at a methane conversion of at least 60%), and high production rate (about 1900 mol kg<sup>-1</sup> h<sup>-1</sup> for H<sub>2</sub>). The energy efficiency of the process was at least 15% [45].

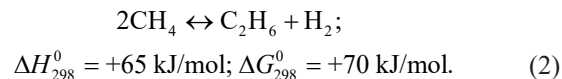
The reaction was carried out under intense light irradiation (*I* = 19.2 W/cm<sup>2</sup>). Due to the high thermal conductivity of the Ru–Cu alloy, the photocatalyst surface was heated to 727°C. At this temperature, the Ru<sub>n</sub>–Cu<sub>n</sub>/MgO–Al<sub>2</sub>O<sub>3</sub> photocatalyst prepared from the nanoparticles of two metals (Ru and Cu) rapidly coked and deactivated—unlike the Ru<sub>1</sub>@Cu<sub>n</sub> single-atom alloy.

The Ru<sub>1</sub>@Cu<sub>n</sub>/MgO–Al<sub>2</sub>O<sub>3</sub> single-atom catalyst exhibited its superior performance only when the synergy of light and heat existed. In contrast, when the reactor was heated to 727°C under dark conditions of thermal catalysis, the catalyst exhibited an almost five-fold lower initial activity in reaction (1). In this case, it demonstrated a low selectivity towards the desired product and completely deactivated very quickly.

#### PHOTOINDUCED NONOXIDATIVE COUPLING OF METHANE

Nonoxidative coupling of methane (NOCM) into C<sub>2</sub> hydrocarbons and hydrogen (reaction (2)) is another

attractive pathway for the productive utilization of natural gas. However, like DRM, this endothermic reaction faces severe thermodynamic limitations [87]. A number of studies have attempted to overcome these limitations using photocatalytic techniques [32, 33, 88].



The engineering implementations of photocatalytic NOCM proposed to date differ in the following aspects: reactor type (flow-type reactors [89, 90], batch reactors [90–92], slurry reactors [93, 94], or chemical looping [95]); irradiation type (intense UV radiation [90–97] or concentrated visible-range sunlight [55, 89, 98]); and the type of reaction medium (anhydrous [95–98], liquid water, or water vapor [99–103]). The photon-driven reaction is generally carried out at room temperature and ambient pressure in the presence of hybrid photocatalysts based on metal oxides doped with transition or noble metals [88]. In recent years, particular attention has been paid to photocatalysts with single-atom metal sites. The photocatalytic properties of these single-atom hybrid photocatalysts depend both on their composition and on the presence of water in the reaction zone.

Previous research in this area has mostly focused on *photocatalytic NOCM in anhydrous media* [55, 95–98, 104–117]. All these studies note that, although undoped metal oxides (TiO<sub>2</sub>, ZnO, Ga<sub>2</sub>O<sub>3</sub>, WO<sub>3</sub>, In<sub>2</sub>O<sub>3</sub>, CeO<sub>2</sub>, etc.) possess both semiconductor and optical properties, these materials are almost inactive and nonselective in photocatalytic NOCM [55, 96]. It is their modification with metal cocatalysts that generates photocatalytic systems capable of promoting methane conversion at a noticeable rate. Particularly efficient hybrid photocatalysts have been prepared with low concentrations (0.1–0.5%) of metal dopants, clearly due to high dispersion of the metals on the semiconductor surface [52]. A number of successful attempts to dope oxide semiconductors (WO<sub>3-x</sub>, TiO<sub>2</sub>, Ga<sub>2</sub>O<sub>3</sub>, Ga–TiO<sub>2</sub>–SiO<sub>2</sub>, and NaTaO<sub>3</sub>) with metal nanoparticles and nanoclusters (specifically, Au, Ag, Pt, and Cu) have been reported to date. However, although these photocatalytic systems exhibited 88–100% selectivity in the formation of C<sub>2</sub> hydrocarbons from methane, their activity was inadequate in most cases (3.5–388 μmol kg<sup>-1</sup> h<sup>-1</sup> with respect to CH<sub>4</sub>) [89, 90, 104–109]. Single-atom photocatalysts have achieved notably higher performance in NOCM, up to a

specific ethane/ethylene yield of 450–1100  $\mu\text{mol g}^{-1} \text{h}^{-1}$  [112, 113, 117].

Most single-atom photocatalysts reported to be applied for NOCM are monometallic (Table 1, items 1–18, 23). They are prepared by immobilizing isolated atoms of transition metals (e.g., Zn [91], Ga, Fe [92], Nb, Mo, and W [110]) or noble metals (e.g., Pd, Pt, Au, Ag, and Ru [55, 96, 111–113]) on the surface of hierarchical macro–mesoporous zeolites or metal oxides. The metal dopant is preferably deposited on the surface of an oxide semiconductor (e.g., the oxide of titanium [55, 112], zinc [89, 101, 117], gallium [96], or indium [113]) that has a nanostructured morphology (nanosheets [89, 112, 117] or nanorods [100, 115]). Alternatively, monometallic single-atom photocatalysts can be prepared in the form of porous titanosilicate ( $\text{TiO}_2\text{-SiO}_2$ ) filmed microarrays: in methane conversion, these two-dimensional thin-film heterogeneous catalysts enhance the light–reactant interaction to a greater extent than even nanostructured materials [110, 111]. Despite the inactivity of titanosilicate films themselves in photocatalytic NOCM, the single-atom photocatalysts prepared by the localization of metal atoms in their macropores exhibit a 15–600-fold higher methane conversion than pristine  $\text{TiO}_2\text{-SiO}_2$  cells. The specific effect depends both on the dopant type (transition or noble metal) and on the manner it affects the photocatalyst bandgap. Specifically, transition metal dopants (Fe, Cu, and Ga), which increase the hole conductivity of the contact, have an almost zero effect on its photocatalytic properties. In contrast, metal dopants that increase the electron conductivity of the microarray ( $\text{Nb} > \text{Mo} > \text{W} > \text{Ta}$ ) enhance both the activation of  $\text{CH}_4$  molecules and the desorption of reaction products ( $\text{C}_2\text{H}_6$  and  $\text{H}_2$ ) [110]. However, regardless of the pathway by which the metal affects the bandgap, the activity of noble-metal-doped microarrays is always more than an order of magnitude higher than that of similar systems doped with transition metals (cf.  $\text{Pt}_1@ \text{TiO}_2\text{-SiO}_2$  [111] vs.  $\text{Nb}_1@ \text{TiO}_2\text{-SiO}_2$  [110], see items 4 and 16 in Table 1).

Noble-metal-doped single-atom photocatalysts based on the most common semiconductors (i.e., titanium, zinc, and gallium oxides) have been thoroughly investigated in photocatalytic NOCM [55, 96, 112, 115]. Using the case of Pd doping, it has been shown for each of these semiconductors that noble metal decoration produces ethane-selective (85–97%) single-atom photocatalysts. On the other hand, their catalytic activities noticeably differ from one another; actually, they increase in the

following order:  $\text{Pd}_1@ \text{Ga}_2\text{O}_3 \ll \text{Pd}_1@ \text{ZnO} \ll \text{Pd}_1@ \text{TiO}_2$ . Table 1 (items 6, 8 and 17) clearly shows that the  $\text{TiO}_2$ -based catalyst exceeds the other two competitors by 1–3 orders of magnitude. When titanium oxide is doped with noble metals, the resultant single-atom photocatalysts can be divided into two types: (1) SACs with diverse particle sizes, which simultaneously include both isolated metal atoms ( $M_1$ ) and metal nanoparticles/nanoclusters ( $M_n$ ) [55]; and (2) catalysts with only single atoms of the metal dopant ( $M_1$ ) on the heterogeneous surface [112].

The photocatalytic systems with diverse particle sizes,  $M_1+M_n/\text{TiO}_2$  ( $M = \text{Pd, Pt, Au, Ag, Ru, Ir, or Rh}$ ), are described in [55]. Although the NOCM activity of these systems depends on the choice of metal dopant (it increases in the order of  $\text{Rh} < \text{Pt} < \text{Ir} < \text{Pd} < \text{Ru} < \text{Ag} < \text{Au}$ ), all of them promote the visible-light-driven conversion of methane to ethane and achieve high selectivity (95–97%) under mild conditions (room temperature and ambient pressure). In all cases, however, these catalysts provide inadequate yields of the desired  $\text{C}_2\text{H}_6$  product (4–82  $\mu\text{mol g}^{-1} \text{h}^{-1}$ ), even when the most effective gold-doped system, namely  $\text{Au}_1+\text{Au}_n/\text{TiO}_2$ , is used (Table 1, items 9–15).

The photocatalytic performance of single-atom photocatalysts that contain only isolated noble metal atoms ( $M_1@ \text{TiO}_2$ ) is manyfold higher than that of systems with diverse dispersion of dopant particles ( $M_1+M_n/\text{TiO}_2$ ) (cf. items 12 vs. 17, Table 1). The order of photocatalytic activity of the dopants is also different in the case of SACs:  $\text{Ru} < \text{Rh} < \text{Ir} \ll \text{Au} \ll \text{Pd}$ , with palladium in the leading position [112]. This order of  $M_1@ \text{TiO}_2$  photocatalytic performance correlates with the degree of occupation of the  $\text{TiO}_2$  valence band by the noble metal  $d$ -orbitals (Fig. 3a) [112] (the valence band is responsible for the hole conductivity of the system, and doping the photocatalyst with noble metal nanoclusters [ $M_n/\text{TiO}_2$ ] enhances the electron conductivity). Different metal impurities have different effects on the properties of a prepared  $M_1@ \text{TiO}_2$  hybrid semiconductor, including its bandgap width and the number of the charged oxygen sites involved in hole conductivity [118, 119]. In all cases, however, the generation of a single-atom metal contact gives rise to the appearance of new positively charged metal carriers ( $M^{\delta+}$ ). In other words, doping  $\text{TiO}_2$  with single-atom metal sites provides conditions for the activation of  $\text{CH}_4$  on positive metal sites ( $M^{\delta+}$ ) rather than on the charged oxygen sites in the  $\text{TiO}_2$  lattice, thus altering the oxidation pathway. In the case of the

**Table 1.** Photoinduced NOCM over single-atom photocatalysts in anhydrous medium (at room temperature and ambient pressure)<sup>a</sup>

Item	Photocatalyst	Reactor type <sup>b</sup>	Illumination conditions <sup>c</sup>	Specific reaction rate, $\mu\text{mol}_{\text{CH}_4} \text{g}^{-1} \text{h}^{-1}$	Selectivity %		$\text{H}_2/\text{C}_2\text{H}_4$	Other products	Energy efficiency, %	References
					$\text{C}_2\text{H}_6$	$\text{C}_2\text{H}_4$				
1	$\text{Zn}^{2+/+}$ -ZSM-5	A	–	~20	99	–	1.0	–	0.55	[91]
2	$\text{Ga}^{3+}$ -ETS-10 <sup>d</sup>	A	150W Hg, $\lambda < 390 \text{ nm}$ , $I = 0.1 \text{ W/cm}^2$	17	>70	8	1.0	–	–	[92]
3	$\text{Fe}^{3+}$ -ETS-10 <sup>d</sup>	A	150W Hg, $\lambda < 390 \text{ nm}$ , $I = 0.1 \text{ W/cm}^2$	30	>70	–	1.0	$\text{C}_3\text{H}_8$ (16%), $\text{C}_4\text{H}_{10}$ (6%)	–	[92]
4	$\text{Nb}_1@/\text{TiO}_2\text{-SiO}_2$	A	300 W Xe	4	96	–	0.9	$\text{C}_3\text{H}_8$	–	[110]
5	Ag-HPW/ $\text{TiO}_2$ <sup>e</sup>	CL	Hg-Xe, $\lambda = 280\text{--}400 \text{ nm}$ , $I = 0.038 \text{ W/cm}^2$	46	77–90	–	–	$\text{C}_3\text{H}_8$ , $\text{CO}_2$	>3.5	[95]
6	$\text{Pd}_1@/\text{Ga}_2\text{O}_3$	B (47°C)	Hg, $\lambda = 254 \text{ nm}$ , $I = 0.02 \text{ W/cm}^2$	<1	–	–	–	–	–	[96]
7	$\text{Pd}_1\text{-Bi}_1@/\text{Ga}_2\text{O}_3$	B (47°C)	Hg, $\lambda = 254 \text{ nm}$ , $I = 0.020 \text{ W/cm}^2$	>1	97	–	–	–	0.2	[97]
8	$\text{Pd}_1+\text{Pd}_\text{H}/\text{ZnO}$	A	300W Xe, $\lambda = 320\text{--}780 \text{ nm}$ , $I = 1.2 \text{ W/cm}^2$	~6	85	15	–	–	–	[115]
9	$\text{Au}_1+\text{Au}_\text{H}/\text{TiO}_2$	B	300W Xe, AM1.5G filter, $\lambda > 420 \text{ nm}$ , $I = 0.1 \text{ W/cm}^2$	170	95	–	1.0	$\text{C}_3\text{H}_8$	–	[55]
10	$\text{Ag}_1+\text{Ag}_\text{H}/\text{TiO}_2$			76	96	–	–	–	–	
11	$\text{Ru}_1+\text{Ru}_\text{H}/\text{TiO}_2$			36	96	–	–	–	–	
12	$\text{Pd}_1+\text{Pd}_\text{H}/\text{TiO}_2$			28	96	~1	–	–	–	
13	$\text{Ir}_1+\text{Ir}_\text{H}/\text{TiO}_2$			16	96	–	–	–	–	
14	$\text{Pt}_1+\text{Pt}_\text{H}/\text{TiO}_2$			8	96	–	–	–	–	
15	$\text{Rh}_1+\text{Rh}_\text{H}/\text{TiO}_2$			2	96	–	–	–	–	
16	$\text{Pt}_1@/\text{TiO}_2\text{-SiO}_2$	A	300W Xe, $\lambda = 365 \text{ nm}$ , $I = 0.21 \text{ W/cm}^2$	~200	72	–	1.0	–	–	[111]
17	$\text{Pd}_1@/\text{TiO}_2$	A	300W Xe, $\lambda = 350 \text{ nm}$ , $I = 0.6 \text{ W/cm}^2$	1930	94	2	1.0	$\text{CO}_2$ (~4%)	3.05	[112]
18	$\text{Ag}^+-\text{In}_2\text{O}_{3-x}$	A <sup>f</sup>	300W Xe (UV-Vis)	~902	88	–	0.8	$\text{CO}_2$ (12%)	–	[113]
19	$\text{Pd}_1+\text{Pd}_\text{H}/\text{Zn-WO}_{3-x}$	–	300W Xe, $I = 0.5 \text{ W/cm}^2$	~64	17	57–	–	$\text{C}_3\text{H}_6$	–	[98]
20	$\text{Pd}_2\text{-Au}_2/\text{Bi}_2\text{NbO}_5\text{F}$	A	300W Xe, $\lambda > 320 \text{ nm}$ , $I = 0.5 \text{ W/cm}^2$	72	27	63	–	$\text{C}_3\text{H}_8$ , $\text{CO}$	–	[114]
21	$\text{Pd}_1@/\text{Au}/\text{ZnO}$	A	300W Xe, $\lambda = 320\text{--}780 \text{ nm}$ , $I = 1.2 \text{ W/cm}^2$	67	56	40	–	$\text{C}_3\text{H}_6$ , $\text{C}_3\text{H}_8$ , $\text{CO}$	–	[115]
22	$\text{Ru}_1@/\text{Au}_{10}\text{-CeO}_2$	A	LED (325 nm), 300 W Xe, $\lambda = 350\text{--}700 \text{ nm}$	14	~100	–	0.3	–	–	[116]
23	$\text{Au}_1+\text{Au}_\text{H}/\text{ZnO}$	–	UV-Vis ( $\lambda = 350\text{--}700 \text{ nm}$ )	22–2375	90–94	0–4	0.9	$\text{CO}_2$ (6%), $\text{H}_2\text{O}$	–	[117]

<sup>a</sup> Unless otherwise specified in the table.

<sup>b</sup> A—batch reactor; B—flow-type tubular reactor; CL—chemical looping.

<sup>c</sup> Hg—mercury lamp; Xe—xenon lamp; LED—light-emitting diode.

<sup>d</sup> ETS-10 is a microporous zeolite-like nanowire (0.67 nm in diameter) titanosilicate.

<sup>e</sup> HPW—heteropolytungstic acid.

<sup>f</sup> With gas circulation inside reactor.

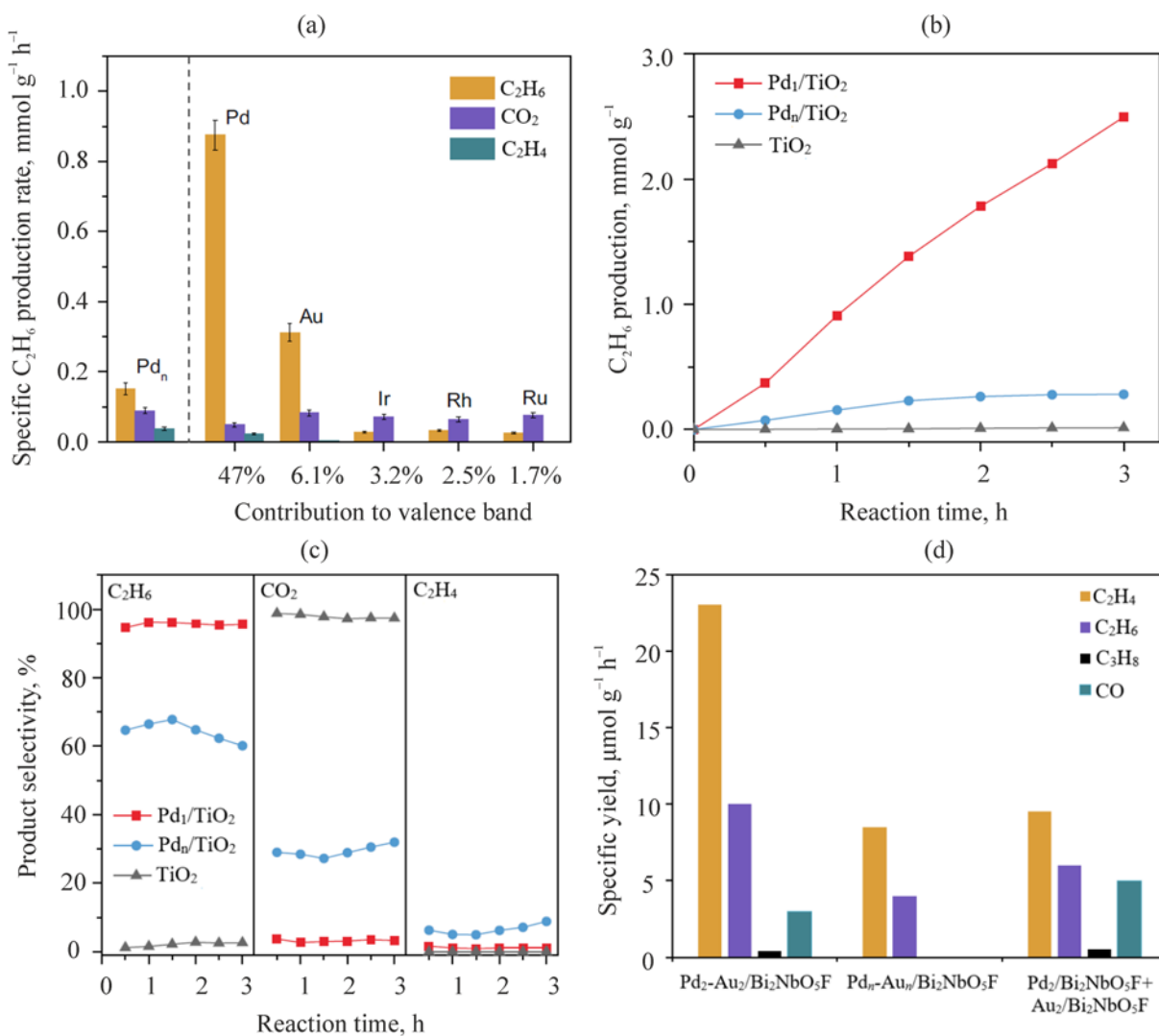


**Fig. 3.** Photocatalytic NOCM performance in presence of: (a)  $M_1@TiO_2$  SACs doped with metals with different contributions to valence band (reproduced from [112]); (b, c)  $Pd_1@TiO_2$ , compared to  $Pd_n/TiO_2$  and  $TiO_2$  (reproduced from [112]); and (d)  $Pd_2-Au_2/Bi_2NbO_5F$ , compared to  $Pd_n-Au_n/Bi_2NbO_5F$  and mechanical mixture  $\{Pd_2/Bi_2NbO_5F + Au_2/Bi_2NbO_5F\}$  (reproduced from [114]). Reaction conditions: room temperature; ambient pressure of  $CH_4$ ; xenon lamp irradiation;  $\lambda = 320-350\ nm$ ;  $I = 0.5-0.6\ W/cm^2$ .

dissociation of methane C–H bonds on oxygen hole sites, the newly-formed methyl radical fragments are electrostatically strongly retained by the charged sites of lattice oxygen, thus directing the process towards the preferential formation of carbon oxides. In contrast, in single-atom photocatalysts, positive noble metal atoms become the key sites for the NOCM reactions. These sites both promote the oxidative activation of  $CH_4$  and provide the stabilization of methyl radicals followed by their coupling into ethane ( $CH_4 + M^{\delta+} \rightarrow [^{\bullet}CH_3 \cdots M^{\delta+}] \rightarrow [C-C-M^{\delta+}] \rightarrow C_2H_6$ ). Therefore, the appearance of positive metal sites makes it possible not only to obtain

an active photocatalyst but also to essentially suppress the excessive oxidation of  $CH_4$  by lattice oxygen.

It should be noted that the presence of isolated positive metal sites and the stabilization of methyl radicals on them during  $CH_4$  activation are typical of SACs, which is what makes them efficient in thermal catalysis [5, 120]. Photocatalytic conditions further enhance their effects because, under photoirradiation, photogenerated holes are concentrated on  $M^{\delta+}$  sites, thus decreasing the NOCM energy barrier many times over and allowing for the reactions to occur even at moderate and low temperatures. For example, in the presence of  $Pd_1@TiO_2$ , switching from

thermal catalysis to photocatalytic conditions decreased the NOCM activation energy by a factor of about 18 (from 167.9 to 9.54 kJ/mol) [112]. This SAC, almost inactive in thermal catalysis, exhibited a very high C<sub>2</sub>H<sub>6</sub> production rate (about 910 μmol g<sup>-1</sup> h<sup>-1</sup>) and 94% selectivity in photocatalytic NOCM at room temperature and ambient pressure. The amount of hydrogen produced matches the NOCM stoichiometry: hydrogen was formed on the photogenerated electron carriers of the photocatalyst due to the reduction of H<sup>+</sup> protons; the protons, in their turn, were formed, along with CH<sub>3</sub> radicals, on the photogenerated holes as a result of C–H dissociation in the methane molecules (CH<sub>4</sub> + h<sup>+</sup> → H<sup>+</sup> + •CH<sub>3</sub>; 2H<sup>+</sup> + e<sup>-</sup> → H<sub>2</sub>). The observed photocatalytic activity was proportional to the light intensity, thus confirming the activation of CH<sub>4</sub> on photogenerated carriers.

Compared both to pristine TiO<sub>2</sub> and to the titanium oxide doped with metal nanoparticles (Pd<sub>n</sub>/TiO<sub>2</sub>), the Pd-doped SAC (Pd<sub>1</sub>@TiO<sub>2</sub>) demonstrated extraordinary performance in photocatalytic NOCM (Figs. 3b, 3c) [112]. The researchers attribute this high efficiency to the fact that a Pd–O<sub>4</sub> unit was constructed in the photocatalyst lattice, implying the potential of accumulating photogenerated holes on the metal sites. This unit results from a chemical interaction between the isolated palladium atoms and the lattice oxygen of TiO<sub>2</sub>, and cannot be obtained with metal nanoparticles. In the case of Pd<sub>n</sub>/TiO<sub>2</sub>, Pd nanoparticles are localized on the titanium oxide surface. Under photocatalytic conditions, the photogenerated electrons would be concentrated at Pd due to the formation of a Schottky junction, while the photogenerated holes would remain in TiO<sub>2</sub> [112]. In Pd<sub>n</sub>/TiO<sub>2</sub>, like in pristine titanium oxide, methane activates on the TiO<sub>2</sub> oxygen sites, which does not entirely rule out the possibility of the formation of carbon oxides during the process (with CO<sub>2</sub> selectivity of about 32%). On the other hand, negative Pd particles can stabilize methyl radicals •CH<sub>3</sub> (produced by the oxidative dissociation of the C–H bonds of CH<sub>4</sub>), thus directing the process toward the production of C<sub>2</sub> hydrocarbons. Although Pd<sub>n</sub>/TiO<sub>2</sub> provided a relatively low yield of C<sub>2</sub> hydrocarbons (about 210 μmol g<sup>-1</sup> h<sup>-1</sup>, which was markedly lower than that on the SAC sample), the reaction products contained not only ethane but also ethylene, a higher value-added hydrocarbon product (Fig. 3c). In the presence of Pd<sub>n</sub>/TiO<sub>2</sub> (the catalyst that only contained Pd nanoparticles), the ethylene selectivity was not high (9% C<sub>2</sub>H<sub>4</sub>, 59% C<sub>2</sub>H<sub>6</sub>).

A series of studies describe Pd-doped bimetallic hybrid photocatalysts that exhibit a C<sub>2</sub>H<sub>4</sub> selectivity of 40 to 75% (items 19–21 in Table 1) [98, 114, 115]. The complex compositions of these photocatalytic systems consisted of highly dispersed palladium coupled with zinc or gold deposited on a metal oxide surface: Pd<sub>1</sub>+Pd<sub>n</sub>/Zn–WO<sub>3-x</sub> [98], Pd<sub>2</sub>–Au<sub>2</sub>/Bi<sub>2</sub>NbO<sub>5</sub>F [114], and Pd<sub>1</sub>@Au/ZnO [115]. Despite the relatively low rate of the photocatalytic reactions (about 60–70 μmol g<sup>-1</sup> h<sup>-1</sup> with respect to CH<sub>4</sub>), these catalysts achieved a total selectivity towards C<sub>2</sub> hydrocarbons of about 90–96%, with the rest reaction products being C<sub>3</sub> hydrocarbons and CO. The product distribution between ethylene and ethane largely depends on palladium dispersion. Specifically, the Pd-doped single-atom photocatalysts (Pd<sub>1</sub>@Au/ZnO) provide for the preponderance of ethane in the reaction products (40% C<sub>2</sub>H<sub>4</sub>, 56% C<sub>2</sub>H<sub>6</sub>) [115]; the systems with palladium nanoclusters/nanoparticles are more selective towards ethylene (57–75% C<sub>2</sub>H<sub>4</sub>, 17–27% C<sub>2</sub>H<sub>6</sub>) [98, 114]. Using a PdAu/Bi<sub>2</sub>NbO<sub>5</sub>F system, Tang et al. [114] demonstrated that photocatalysts with dual (Pd + another metal) atomic sites (Pd<sub>2</sub>–Au<sub>2</sub>/Bi<sub>2</sub>NbO<sub>5</sub>F) achieve the highest efficiency in C<sub>2</sub>H<sub>4</sub> production. However, their superiority is manifested only when the atomic sites of these two metals are chemically bound, because a mechanical mixture of dual monometallic photocatalysts (Pd<sub>2</sub>/Bi<sub>2</sub>NbO<sub>5</sub>F+Au<sub>2</sub>/Bi<sub>2</sub>NbO<sub>5</sub>F) is inefficient and its photocatalytic properties are similar to those of a Pd<sub>n</sub>–Au<sub>n</sub>/Bi<sub>2</sub>NbO<sub>5</sub>F system composed of metal nanoparticles (Fig. 3d). These dual bimetallic sites were found to implement the tandem photocatalytic strategy, with the CH<sub>4</sub> to C<sub>2</sub>H<sub>6</sub> conversion occurring on Au sites and ethane being dehydrogenated to ethylene on Pd sites.

The synergy of two active sites during photocatalytic NOCM has also been observed for Pd–Zn-loaded polymetallic systems (Pd<sub>1</sub>+Pd<sub>n</sub>/Zn–WO<sub>3-x</sub> [98] and Pd<sub>1</sub>@Au/ZnO [115]) based on oxide semiconductors (WO<sub>3-x</sub>, ZnO). The hybrid photocatalytic system additionally included plasmonic components (gold nanoparticles or tungsten oxide with a defective lattice) to improve the optical properties of the photocatalyst, facilitate the separation of photogenerated carriers, and promote the generation of methane activation sites (Zn<sup>+</sup>–O<sup>-</sup>) from Zn<sup>2+</sup> and lattice oxygen (O<sup>2-</sup>). The hypothetical scheme (Fig. 4) [115] shows that methane is converted to ethylene through alkoxy intermediates, with palladium, zinc, and lattice oxygen being cooperatively involved. Under photoirradiation, electrons are transferred from the

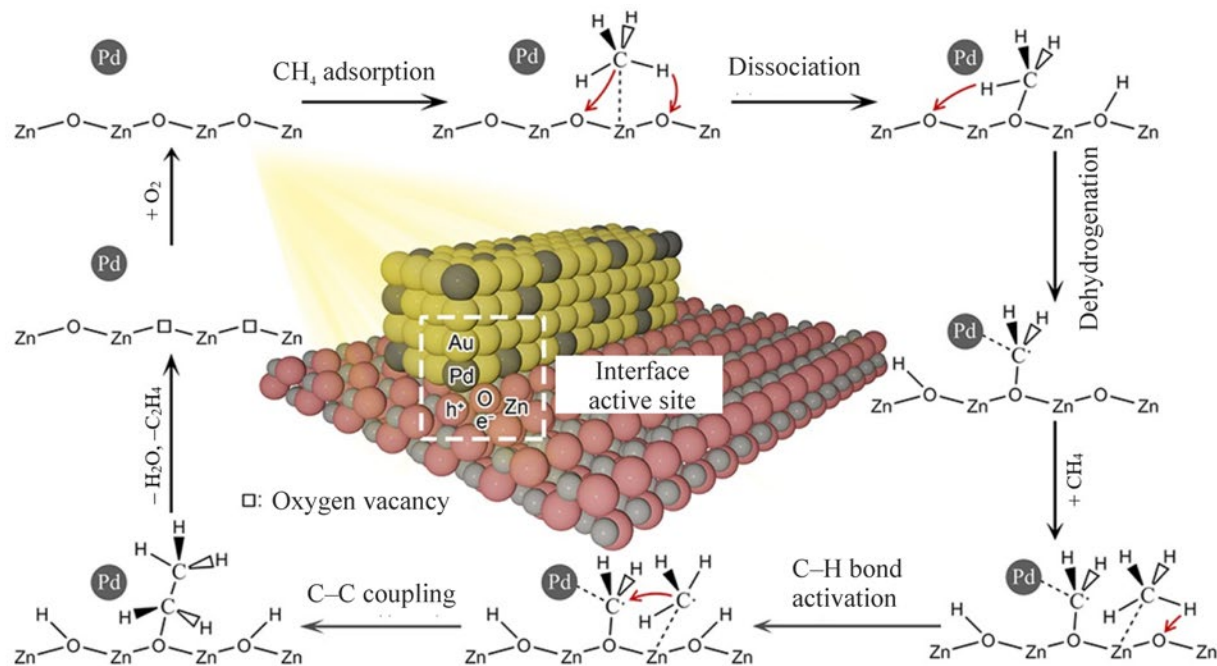


**Fig. 4.** Schematic illustration of photocatalytic CH<sub>4</sub>-to-C<sub>2</sub>H<sub>4</sub> conversion through surface alkoxy intermediates over Pd<sub>1</sub>@Au/ZnO hybrid photocatalyst (reproduced from [115]).

oxygen atom to the zinc atoms, thus generating paired Zn<sup>+</sup>-O<sup>-</sup> sites, on which methane undergoes dissociative adsorption to form a methoxy derivative (\*OCH<sub>3</sub>). With cooperation from the palladium site, this intermediate becomes stabilized, thus preventing its further oxidation to carbon oxides. Due to its dehydrogenating ability, palladium promotes the subsequent conversion of the methoxy intermediate to C<sub>2</sub>H<sub>4</sub> through an ethoxy derivative (\*OCH<sub>2</sub>CH<sub>3</sub>).

A number of recent publications report on the achievement of high ethylene selectivity in the presence of Pd-free hybrid composite photocatalysts prepared by doping highly dispersed gold into tungsten oxide (Au<sub>*n*</sub>/WO<sub>3-*x*</sub> [107]) and carbonized zinc oxide (Au<sub>*n*</sub>/C-ZnO [109]). In the first case, it was found that, under photocatalytic conditions, a local electric field is induced on Au sites, and hot electrons are generated and involved in the CH<sub>4</sub>-to-C<sub>2</sub>H<sub>6</sub> conversion through the methyl intermediate (\*CH<sub>3</sub>) on negative Au<sup>δ-</sup> sites [107]. Negative oxygen sites (O<sup>-</sup>), generated under the impact of photons from the lattice oxygen atoms of the oxide photocatalyst, are responsible for high ethylene selectivity: the methyl radicals immobilized on the O<sup>-</sup> sites promote the alkoxy pathway [107, 109]. Although the Au<sub>*n*</sub>/WO<sub>3-*x*</sub>

photocatalyst, with oxygen defects in the tungsten oxide lattice, provides 100% methane-to-ethylene selectivity (at room temperature, ambient pressure, and under visible light irradiation), it exhibits a very low activity (indicated by a specific reaction rate not exceeding 6 μmol<sub>CH<sub>4</sub></sub> g<sup>-1</sup> h<sup>-1</sup> [107]). The methane-to-ethylene conversion activity of Au<sub>*n*</sub>/C-ZnO is markedly higher (about 46 μmol<sub>C<sub>2</sub>H<sub>4</sub></sub> g<sup>-1</sup> h<sup>-1</sup> with 99% selectivity) [109]. This performance is achieved by stabilizing oxygen atoms in the crystal lattice via carbon-doping of ZnO.

The catalytic systems prepared from non-carbonized zinc oxide and highly dispersed gold (Au<sub>*n*</sub>/ZnO or Au<sub>1</sub>+Au<sub>*n*</sub>/ZnO) have been selective towards ethane rather than ethylene. A number of publications report on attempts to use these catalysts in photoinduced NOCM [89, 107, 115, 117]. Despite the high C<sub>2</sub>H<sub>6</sub> selectivity (90–94%) reported in all these papers, the published data on the activity of these photocatalysts are rather controversial. Most papers note the low activity of Au<sub>1</sub>+Au<sub>*n*</sub>/ZnO photocatalytic systems (a specific C<sub>2</sub>H<sub>6</sub> yield of about 10–11 μmol g<sup>-1</sup> h<sup>-1</sup>), with ethylene being the dominant byproduct (up to 4%) [89, 107, 115]. On the other hand, Zheng et al. [117] describe the preparation of a seemingly similar composite that has an activity two

orders of magnitude higher than that reported in the other references (a C<sub>2</sub>H<sub>6</sub> yield of 1122 μmol g<sup>-1</sup> h<sup>-1</sup>), with the byproducts consisting of CO<sub>2</sub> and traces of H<sub>2</sub>O rather than ethylene. This, along with the appearance of oxygen vacancies in the oxide lattice during the process, serves as evidence of the instability of lattice oxygen. They explain the record activity of their photocatalytic system by the generation of two negative sites (Au<sup>δ-</sup> and O<sup>-</sup>) on the photocatalyst surface: these sites, together, are assumed to polarize very effectively the C–H bonds of methane and to promote further methane transformations. We believe, however, that this explanation of the extraordinary photocatalytic activity appears rather doubtful. Attention should be drawn to the water traces detected in the reaction products: this could alter the photocatalytic mechanism and enhance the process performance [100–103].

A series of publications have been related to *photocatalytic NOCM in the presence of water* [93, 94, 99–103]. Their data are summarized in Table 2.

References [99, 100] propose photo-driven NOCM in an aqueous solution of Fe<sup>3+</sup> salts or in the presence of water vapor over magnesium oxide/alumina doped with highly dispersed nickel (Ni<sup>2+</sup>-MgO/Al<sub>2</sub>O<sub>3</sub>). A major disadvantage of photocatalytic systems of this kind is their poor energy efficiency, not exceeding 0.21% (Table 2, items 1, 2).

The photocatalysts doped with noble metals (Table 2, items 3–7) have an order of magnitude higher efficiency than the other materials. Among them, researchers have most often used conventional semiconductors (e.g., oxides of titanium, zinc, or gallium) doped with highly dispersed palladium or platinum with single-atom metal sites (Pt<sub>1</sub>@Ga<sub>2</sub>O<sub>3</sub>, Pd<sub>1</sub>@Ga<sub>2</sub>O<sub>3</sub>, and Pd<sub>1</sub>@ZnO) [101–103] or with diversely dispersed sites (Pt<sub>1</sub>+Pt<sub>n</sub>/TiO<sub>2</sub>, Pd<sub>1</sub>+Pd<sub>n</sub>/TiO<sub>2</sub>, and Pd<sub>1</sub>+Pd<sub>n</sub>/ZnO) [93, 94, 101]. Using these photocatalytic systems, the NOCM reactions have been investigated under intense UV irradiation and continuous flow conditions, which have been implemented either in a slurry reactor with an aqueous medium [93, 94, 101] or in a fixed-bed reactor in the presence of water vapor [102, 103]. All the researchers have noted that introducing water into the reaction zone leads to a manyfold increase in the yield of ethane (Fig. 5a). It should be emphasized that the effect of H<sub>2</sub>O addition depends not so much on the choice of metal dopant as on the semiconductor properties. In particular, the wider the oxide's bandgap, the stronger this effect (TiO<sub>2</sub> < ZnO < Ga<sub>2</sub>O<sub>3</sub>), which indicates that oxides are

not strongly involved in methane activation. The presence of water completely reverses the order of activity of the catalysts in NOCM: the highest performance was achieved for Pd<sub>1</sub>@Ga<sub>2</sub>O<sub>3</sub> [102], a SAC that remains almost inactive in anhydrous media [96] (cf. item 6 in Table 1 vs. item 7 in Table 2). All this points to a likely change in the catalytic cycle and to the involvement of water molecules.

Some researchers regard water as a cocatalyst in photocatalytic NOCM via indirect activation of CH<sub>4</sub> molecules [93, 94, 121]. A series of experiments on the effects of carrier traps on process performance have shown that, like in anhydrous media, the oxidative activation of methane and the reductive formation of hydrogen occur on photogenerated holes (h<sup>+</sup>) and electrons (e<sup>-</sup>), respectively [93, 94]. However, Sato et al. [121] demonstrated (using real-time mass spectrometry and *operando* IR spectroscopy) that, in the presence of even traces of H<sub>2</sub>O, the reactions occur on h<sup>+</sup> sites in the following sequence: aqueous hydroxyl radicals are oxidized into •OH radicals, which subsequently affect the C–H bonds of CH<sub>4</sub> molecules, thus being directly involved in the formation of methyl intermediates (•CH<sub>3</sub>). Given that H<sub>2</sub>O exceeds methane in kinetic activity [121], the dissociation of C–H bonds ceases to limit the NOCM reactions, resulting in their manyfold acceleration. Water not only catalyzes the oxidative dissociation of C–H bonds but also promotes the subsequent pairing of •CH<sub>3</sub> radicals into C<sub>2</sub>H<sub>6</sub> on the surface of a heterogeneous catalyst [90, 121]. The presence of •OH and •CH<sub>3</sub> radicals in the photocatalytic methane conversion in the presence of H<sub>2</sub>O has been reliably confirmed by electron paramagnetic resonance (EPR) spectra [94].

A radical process theoretically involves a large number of reactions [93, 94]. For example, the following transformations potentially occur in photocatalytic NOCM over Pt<sub>1</sub>+Pt<sub>n</sub>/TiO<sub>2</sub>:

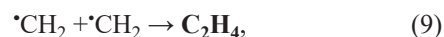
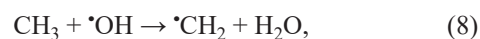
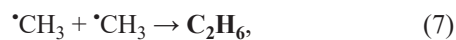
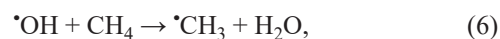
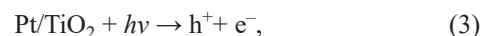
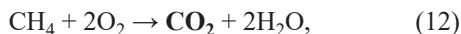
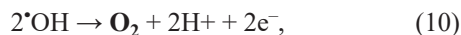


**Table 2.** Photoinduced NOCM over single-atom photocatalysts in aqueous medium or in the presence of water vapor (at room temperature and ambient pressure)<sup>a</sup>

Item	Photocatalyst	Reactor type <sup>b</sup>	Illumination conditions <sup>c</sup>	Specific reaction rate, $\mu\text{molCH}_4\text{g}^{-1}\text{h}^{-1}$	Selectivity %		$\text{H}_2/\text{C}_2\text{H}_4$	Other products	Energy efficiency, %	References
					$\text{C}_2\text{H}_6$	$\text{C}_2\text{H}_4$				
1	$\text{Fe}(\text{NO}_3)_3$ ( $\text{Fe}^{3+}$ )	A	LED, $\lambda = 395$ nm, $I = 0.45$ W/cm <sup>2</sup>	18	94	<1	—	CO <sub>2</sub> (5%), CH <sub>3</sub> OH	—	[99]
2	$\text{Ni}^{2+}$ -MgO/Al <sub>2</sub> O <sub>3</sub>	B (150°C)	300W Xe, $\lambda \geq 350$ nm, $I = 1.0$ W/cm <sup>2</sup>	929	98	1.8	—	CO <sub>2</sub> (2%), O <sub>2</sub>	0.21 <sup>d</sup>	[100]
3	$\text{Pd}_1 + \text{Pd}_n/\text{TiO}_2$	C	Hg (UV), $\lambda = 254$ nm	76	73	—	1.1	CO <sub>2</sub> (27%)	2.8 <sup>d</sup>	[93]
4	$\text{Pt}_1 + \text{Pt}_n/\text{TiO}_2$	C	Hg (UV), $\lambda = 254$ nm	144	62	~2	2.0	CO <sub>2</sub> (33%), CO	3.3 <sup>d</sup>	[94]
5	$\text{Pd}_1 + \text{Pd}_n/\text{ZnO}$	B (60°C)	450W Hg (UV)	946–2190	45–46	~2	—	CO <sub>2</sub> (52%), CO	—	[101]
6	$\text{Pt}_1 @ \text{Ga}_2\text{O}_3$	B (3.6 kPa water vapor) (3.0 kPa water vapor, 200 kPa CH <sub>4</sub> )	40W Hg, $\lambda = 254$ nm, $I = 0.014$ W/cm <sup>2</sup>	1091	22	—	—	CO <sub>2</sub> (67%), CO	—	[102]
7	$\text{Pd}_1 @ \text{Ga}_2\text{O}_3$	B (3.6 kPa water vapor)	40W Hg, $\lambda = 254$ nm, $I = 0.014$ W/cm <sup>2</sup>	2495	76–80	—	—	CO <sub>2</sub> (35%), CO	—	[103]
							3.2	CO <sub>2</sub> (23%), CO	5.1 <sup>d</sup> 11.6–14.4 <sup>e</sup>	[102]

<sup>a</sup> Unless otherwise specified in the table.<sup>b</sup> A—batch reactor; B—flow-type tubular reactor; C—slurry reactor.<sup>c</sup> Hg—mercury lamp; Xe—xenon lamp; and LED—light-emitting diode.<sup>d</sup> Quantum efficiency ( $\text{C}_2\text{H}_6$ ).<sup>e</sup> Quantum efficiency ( $\text{H}_2$ ).



The main reactions are (3) to (7) as they produce ethane and hydrogen. However, the radical process can continue along the pathway of reactions (8) to (10) to additionally give ethylene and oxygen. In its turn, oxygen will potentially involve methane into incomplete oxidation to CO (11) and complete oxidation to CO<sub>2</sub> (12). Carbon dioxide can also be produced at photocatalyst holes by steam reforming of methane (13).

The formation of CO<sub>2</sub> is accelerated in the presence of  $\cdot\text{OH}$  radicals, while the production of C<sub>2</sub>H<sub>6</sub> is facilitated by improving the diffusion characteristics of the photocatalyst and by increasing the CH<sub>4</sub> partial pressure (up to 100–200 kPa) [102, 103].

All the above-listed compounds (H<sub>2</sub>, C<sub>2</sub>H<sub>6</sub>, C<sub>2</sub>H<sub>4</sub>, CO, and CO<sub>2</sub>), in different proportions, have been detected in the reaction products of photocatalytic NOCM processes carried out in aqueous media over various single-atom photocatalysts: Pt<sub>1</sub>+Pt<sub>*n*</sub>/TiO<sub>2</sub> [110], Pd<sub>1</sub>+Pd<sub>*n*</sub>/TiO<sub>2</sub> [94], Pd<sub>1</sub>@ZnO [101], Pd<sub>1</sub>@Ga<sub>2</sub>O<sub>3</sub> [102], Pt<sub>1</sub>@Ga<sub>2</sub>O<sub>3</sub> [103], and Ni<sup>2+</sup>–MgO/Al<sub>2</sub>O<sub>3</sub> [100] (Figs. 5a to 5f). In all the cases, the dominant byproduct was CO<sub>2</sub>, and the amount of hydrogen product was several times higher than the stoichiometry of the target C<sub>2</sub>H<sub>6</sub> production reaction (2).

Water serves as the main source of hydrogen and of CO<sub>2</sub> formation: under photocatalytic conditions, the H<sub>2</sub>O molecule either splits into H<sub>2</sub> and O<sub>2</sub>, or enters steam reforming of methane into H<sub>2</sub> and CO<sub>2</sub> [93, 94]. The negligible methane conversion observed in the absence of water under the process conditions imposed in these studies (Fig. 5b) suggests that an aqueous medium creates a synergistic effect of several NOCM reactions. This synergy imparts a relatively high energy efficiency to the photocatalytic process, especially with respect to hydrogen production (up to 14.4%). However, the concurrent CO<sub>2</sub> formation is generally responsible for a lower ethane selectivity (45–80%) than that in anhydrous media.

While Yu et al. [93, 94] note the importance of radical reactions in aqueous-medium photocatalytic NOCM, they deem it possible that, like in anhydrous media, the metal dopant atoms are involved in redox reactions

on photoexcited carriers. This assumption is consistent with the fact that the main photocatalytic regularities remain unchanged even though water is added to the reaction zone. Regardless of the presence or absence of H<sub>2</sub>O, pristine semiconductors are almost inactive, and Pd-doped catalysts achieve the highest yield of ethane (Fig. 5a). In addition, Pd–Zn catalysts promote the formation of some ethylene along with ethane (Fig. 5c). Furthermore, the photocatalytic activity increases with the dopant dispersion and reaches its maximum on SACs, i.e., catalysts in which the active metal consists only of single atoms or cations (Figs. 5c, 5e) [94, 100–102]. Ishimaru et al. [102] confirmed experimentally that the particles of the reduced metal (in particular, Pd) that accumulate the photogenerated electrons are involved in the reductive reactions of H<sub>2</sub> production. The data reported in [99] confirm—for the case of photo-driven NOCM in an aqueous iron nitrate solution—that metal cations that contain photogenerated holes can be involved in the oxidative dissociation of the methane C–H bonds.

Zhang et al. [99] constructed a full redox cycle for CH<sub>4</sub> conversion with the production of C<sub>2</sub>H<sub>6</sub> and H<sub>2</sub> in the presence of Fe<sup>3+</sup> ions. They found that, in a system of this kind, CH<sub>4</sub> coupling is induced by hydroxyl radicals that are generated by photo-driven intermolecular charge migration of an Fe<sup>3+</sup> complex. The delicate coordination structure of the [Fe(H<sub>2</sub>O)<sub>5</sub>OH]<sup>2+</sup> complex ensures selective C–H bond activation and C–C coupling of CH<sub>4</sub>. The Fe<sup>2+</sup> produced by Fe<sup>3+</sup> reduction is involved in the reductive reactions of electrolytic H<sub>2</sub> production, thus turning back into Fe<sup>3+</sup> and closing the catalytic cycle. This process design almost completely precludes the formation of CO<sub>2</sub>, thus providing high ethane selectivity (94%). However, the C<sub>2</sub>H<sub>6</sub> formation rate is low (8.4 μmol h<sup>−1</sup>), in particular due to the lack of reaction synergies.

Turning back to photocatalytic NOCM over heterogeneous catalysts in the presence of H<sub>2</sub>O, where reaction synergy exists, their performance critically depends on two factors, namely the photocatalyst composition (in particular, the type of metal dopant) and the physical form of water in the reaction zone. The dopant determines the ratio between the rates of H<sub>2</sub>O and CH<sub>4</sub> conversion reactions occurring in NOCM, thus affecting both the production rate and selectivity. For example, Pt-doped catalysts—more active in water-involving reactions than their Pd-doped counterparts [11]—generally exhibit a higher methane conversion rate and a lower yield of C<sub>2</sub>H<sub>6</sub> [93, 94, 102, 103]. The physical form of H<sub>2</sub>O is

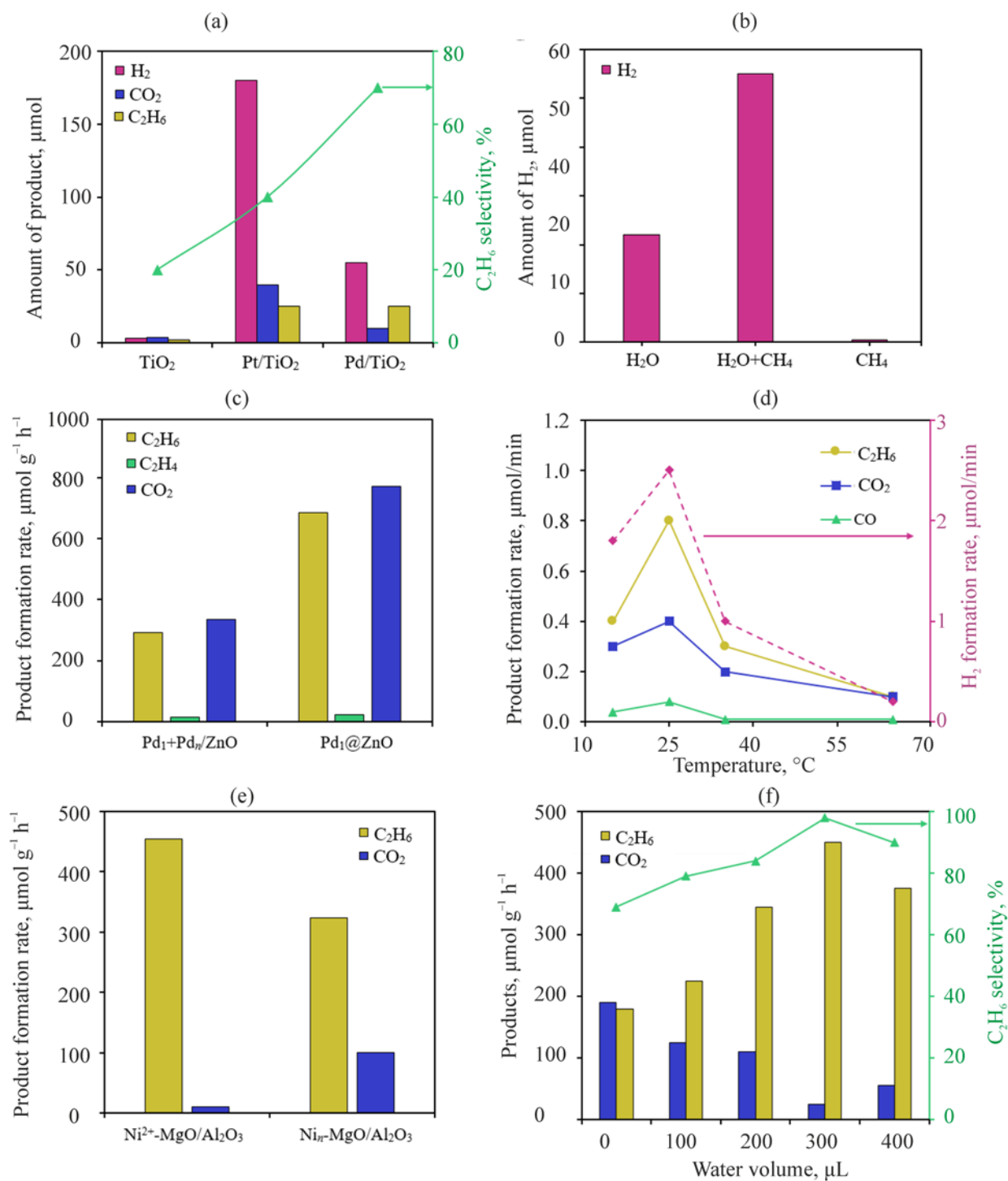


**Fig. 5.** Formation of carbonaceous products and hydrogen in photocatalytic methane conversion over SACs in presence of water, with other conditions being varied: (a) Liquid water, room temperature, photocatalyst composition being varied (based on [11]); (b) Pd<sub>1</sub>+Pd<sub>n</sub>/TiO<sub>2</sub> catalyst, choice of reactants being varied (based on [93]); (c) Liquid water, 60°C, Pd/ZnO photocatalyst, Pd dispersion being varied (based on [101]); (d) Water vapor, Pd<sub>1</sub>@Ga<sub>2</sub>O<sub>3</sub>, temperature being varied (based on [102]); (e) Water vapor, 150°C, Ni dispersion and catalyst type being varied (Ni<sup>2+</sup>-MgO/Al<sub>2</sub>O<sub>3</sub> and Ni<sub>n</sub>-MgO/Al<sub>2</sub>O<sub>3</sub>) (based on [100]); and (f) catalyst Ni<sup>2+</sup>-MgO/Al<sub>2</sub>O<sub>3</sub> with water volume being varied (based on [100]).

also of great importance: the reaction rate is an order of magnitude higher when saturated water vapor is used instead of liquid water [102, 121]. Photoactivated interfacial water particles form a thin film (with a thickness of about 1 nm, or about 3.5 monolayers of H<sub>2</sub>O molecules) on the photocatalyst surface and, as such, participate in NOCM [102, 103, 121]. These adsorbed water molecules provide the reaction field that promotes C<sub>2</sub>H<sub>6</sub> production: specifically, they promote the dissociation of the methane C–H bond as they hydrate and stabilize intermediate hydrocarbon radicals so as to prevent them from subsequent oxidation and to direct the reaction toward ethane formation [102]. The importance of water adsorption on the photocatalyst surface is confirmed by the dependence of ethane formation rate on water vapor pressure and on reaction temperature [102]. In the photocatalytic NOCM over Pd<sub>1</sub>@Ga<sub>2</sub>O<sub>3</sub>, the maximum C<sub>2</sub>H<sub>6</sub> formation rate was achieved in the presence of saturated water vapor (P<sub>H<sub>2</sub>O</sub> = 3.0–3.6 kPa) at room temperature (Fig. 5d). However, this rate abruptly dropped when the temperature either decreased (due to water vapor condensation) or increased (apparently as a result of H<sub>2</sub>O desorption from the heterogeneous surface of the photocatalyst). These trends are typical of other photocatalysts (e.g., Pt/TiO<sub>2</sub>, Pt/NaTaO<sub>3</sub>, and Pt/TiO<sub>2</sub> [121]) as well; in all cases, the coupling of •CH<sub>3</sub> radicals on the surface of water-covered heterogeneous catalysts occurs only at low temperatures (about 40°C) [121].

At higher temperatures, the reaction mainly transitions to the gas phase [121], where no radical generation is observed, and the H<sub>2</sub>O molecules are not directly involved in the CH<sub>4</sub>-to-C<sub>2</sub>H<sub>6</sub> conversion anymore [100]. At the same time, water vapor can also enhance the methane-to-ethane conversion in photothermal coupling [100].

Shen et al. [100] investigated the effects of H<sub>2</sub>O on visible-light-driven photothermal NOCM in the presence of a Ni<sup>2+</sup>-MgO/Al<sub>2</sub>O<sub>3</sub> SAC at 150°C and ambient pressure (Figs. 5e, 5f). In the absence of water vapor, CO<sub>2</sub> and ethane were simultaneously produced from methane in about equal proportions, and the catalyst rapidly lost its activity. An addition of water droplets (0.1–0.4 mL) stabilized the catalyst and markedly suppressed the carbon dioxide formation. Moreover, the yield of C<sub>2</sub>H<sub>6</sub> increased by a factor of about 1.5–2, its peak (454.3 μmol g<sup>-1</sup> h<sup>-1</sup> with about 98% selectivity) corresponding to 0.3 mL of water. As water droplets enter the reaction zone, they vaporize and presumably adsorb on the catalyst surface [100], thus affecting the NOCM process. When H<sub>2</sub>O is added

in greater amounts, it does not vaporize completely, and its effect decreases. Analogous trends were also observed in the presence of similarly composed photocatalyst except that it contained nickel nanoparticles (Ni<sub>n</sub>-MgO/Al<sub>2</sub>O<sub>3</sub>). However, the last one exhibited markedly lower performance values (a C<sub>2</sub>H<sub>6</sub> yield of 260–320 μmol g<sup>-1</sup> h<sup>-1</sup> and a selectivity of about 60–70%) (Fig. 5e).

Unlike catalysts with nanodispersed nickel, a single-atom photocatalyst has single Ni<sup>2+</sup> cations incorporated into its MgO cell by isomorphic substitution of Mg<sup>2+</sup> ions. This creates preconditions for the formation of oxygen sites most enriched with photogenerated electrons. Electrophilic oxygen atoms in the MgO lattice can abstract one hydrogen atom from CH<sub>4</sub> to form the H–O<sub>lattice</sub>–CH<sub>3</sub> structure. The activated methyl intermediate is adsorbed on the O<sub>lattice</sub> site, resulting in further hydrogen dissociation and the consumption of lattice oxygens to eventually generate an over-oxidative CO<sub>2</sub> product. In addition, this adsorption deactivates the photocatalyst. With regard to the mechanism of water vapor effects on photothermal catalysis, water is assumed to perform two functions [100]: (1) as H<sub>2</sub>O splits into H<sub>2</sub> and O<sub>2</sub> gases, it repairs the oxygen defects generated during the reaction process (in accordance with the Mars–van-Krevelen mechanism, with respect to O<sub>2</sub> transfer from the gas phase to the catalyst surface [122]); and (2) in the presence of H<sub>2</sub>O, the CH<sub>3</sub> intermediate activated on oxygen sites migrates onto Ni sites, where it undergoes coupling into C–C bonds, thus giving C<sub>2</sub>H<sub>6</sub>. Due to these functions of water, even trace amounts of H<sub>2</sub>O in the reaction system are able to stabilize active sites and substantially promote ethane production rate and selectivity. The above suggests that lattice oxygen is the only site responsible for the activation of methane C–H bonds (with Ni<sup>2+</sup> ions presumably acting as C–C bond formation sites) [100].

The heterogeneous Ni<sup>2+</sup>-MgO/Al<sub>2</sub>O<sub>3</sub> has become the first noble-metal-free single-atom photocatalyst ever known for NOCM. Moreover, its photocatalytic application at elevated temperatures has to date remained the only example, and a successful one, of catalytic NOCM initiated by photogenerated charge carriers under photothermal conditions. On the other hand, its catalytic performance is at least twofold lower than that achieved by some recently reported single-atom photocatalysts doped with noble metals such as Pd<sub>1</sub>@Ga<sub>2</sub>O<sub>3</sub> [102], Pd<sub>1</sub>@TiO<sub>2</sub> [112], and Au<sub>1</sub>+Au<sub>n</sub>/ZnO [117]. Whether in the presence of water vapor (Pd<sub>1</sub>@Ga<sub>2</sub>O<sub>3</sub>) or in an anhydrous medium (Pd<sub>1</sub>@TiO<sub>2</sub> and Au<sub>1</sub>+Au<sub>n</sub>/ZnO),

these photocatalysts promote NOCM at room temperature under photoirradiation with an intensity of 1–6 suns ( $I = 0.1\text{--}0.6 \text{ W/cm}^2$ ). The specific ethane production rates ( $910\text{--}1122 \mu\text{mol g}^{-1} \text{ h}^{-1}$ ) exhibited by these catalysts are at least comparable to the values achieved by SACs under thermocatalytic conditions at  $650\text{--}700^\circ\text{C}$  [123, 124]. Yet, the methane conversion that has been actually achieved is insufficient for industrial implementation of the process, and the inadequate  $\text{C}_2\text{H}_6$  quantum efficiency (not exceeding 5.1%) should also be taken into account. However, we believe that this type of photocatalysts holds promise for their further development, for example, using advanced optical techniques capable of focused irradiation and, thus, of boosting light intensity to several hundred suns. Further research should also take advantage of some other opportunities offered by photothermal catalysis. In particular, paired (acid–base) Lewis sites highly efficient in the activation of methane C–H bonds can be generated on the surface of oxide semiconductors at about  $120\text{--}600^\circ\text{C}$  [125, 126].

## CONCLUSIONS

The literature data discussed in this review show the high application potential of integrated photocatalysis/single-atom catalysis technology for methane chemistry:

—State-of-the-art photocatalytic methods based on the use of highly dispersed metal-doped hybrid photocatalysts make it possible to overcome thermodynamic limitations and, thus, carry out NOCM and DRM reactions without external heating;

—Single-atom photocatalysts have proven to be more efficient than catalysts doped with metal nanoparticles or nanoclusters. This is most likely attributable to the advantageous photocatalytic properties of SACs, such as the accumulation of photogenerated holes and the involvement of positive metal sites in the oxidative dissociation of methane C–H bonds, as well as the relative stabilization of methyl intermediates. The last feature promotes the coupling of the methyl radicals into  $\text{C}_2\text{H}_6$  (under NOCM reaction conditions); and

—Bimetallic systems such as single-atom alloys with the second metal represented by nanoparticles with enhanced plasmonic photosensitivity appear to hold the greatest promise.

## AUTHOR INFORMATION

N.N. Ezhova, ORCID: <https://orcid.org/0000-0001-5993-7277>

K.B. Golubev, ORCID: <https://orcid.org/0000-0001-7183-7324>

Yu.M. Snatenkova, ORCID: <https://orcid.org/0000-0002-6221-4034>

N.V. Kolesnichenko, ORCID: <https://orcid.org/0000-0003-2534-2624>

## FUNDING

This work was carried out within the State Program of TIPS RAS.

## CONFLICT OF INTEREST

The authors declare no conflict of interest requiring disclosure in this article.

## REFERENCES

1. Arshinov, I.S., Zhagfarov, F.G., Mamaev, A.V., and Miroshnichenko, D.A., *Neftegazokhimiya*, 2023, no. 1, pp. 5–10.  
<https://doi.org/10.24412/2310-8266-2023-1-5-10>
2. Cho, Y., Yamaguchi, A., and Miyauchi, M., *Catalysts*, 2021, vol. 11, no. 1, Art. ID: 18.  
<https://doi.org/10.3390/catal11010018>
3. Kolesnichenko, N.V., Ezhova, N.N., and Snatenkova, Yu.M., *Russ. Chem. Rev.*, 2020, vol. 89, no. 2, pp. 191–224.  
<https://doi.org/10.1070/RCR4900>
4. Ezhova, N.N., Kolesnichenko, N.V., and Maximov, A.L., *Petr. Chem.*, 2022, vol. 62, no. 1, pp. 40–61.  
<https://doi.org/10.1134/S0965544122010078>
5. Kolesnichenko, N.V., Ezhova, N.N., and Snatenkova, Yu.M., *Russ. Chem. Rev.*, 2023, vol. 92, no. 5, Art. ID: RCR5079.  
<https://doi.org/10.57634/RCR5079>
6. Tang, Y., Li, Y., and Tao, F.F., *Chem. Soc. Rev.*, 2022, vol. 51, no. 1, pp. 376–423.  
<https://doi.org/10.1039/D1CS00783A>
7. Meng, X., Cui, X., Rajan, N.P., Yu, L., Deng, D., and Bao, X., *Chem.*, 2019, vol. 5, pp. 1–30.  
<https://doi.org/10.1016/j.chempr.2019.05.008>

8. Nkinahamira, F., Yang, R., Zhu, R., Zhang, J., Ren, Zh., Sun, S., Xiong, H., and Zeng, Zh., *Adv. Sci.*, 2023, vol. 10, no. 5, Art. ID: 2204566. <https://doi.org/10.1002/advs.202204566>
9. Qi, Ch., Xing, Y., Yu, H., Bi, Y., Zhou, P., Wu, H., Guo, R., Zhang, H., Wu, M., and Wu, W., *Ind. Eng. Chem. Res.*, 2022, vol. 61, no. 45, pp. 16635–16642. <https://doi.org/10.1021/acs.iecr.2c01823>
10. Mei, D., Zhang, P., Duan, G., Liu, Sh., Zhou, Y., Fang, Zh., and Tu, X., *J. CO<sub>2</sub> Utilization*, 2022, vol. 62, Art. ID: 102073. <https://doi.org/10.1016/j.jcou.2022.102073>
11. Xie, Sh., Ma, W., Wu, X., Zhang, H., Zhang, Q., and Wang, Y., *Energy Environ. Sci.*, 2021, vol. 14, no. 1, pp. 37–89. <https://doi.org/10.1039/D0EE01860K>
12. Hibino, T., Kobayashi, K., Nagao, M., Zhou, D., Chen, S., and Yamamoto, Y., *ACS Catalysis*, 2023, vol. 13, no. 13, pp. 8890–8901. <https://doi.org/10.1021/acscatal.3c01333>
13. Li, X., Wang, C., and Tang, J., *Nat. Rev. Mater.*, 2022, vol. 7, pp. 617–632. <https://doi.org/10.1038/s41578-022-00422-3>
14. Liu, Zh., Xu, B., Jiang, Y.J., Zhou, Y., Sun, X., Wang, Y., and Zhu, W., *ACS Environ. Au*, 2023, vol. 3, no. 5, pp. 252–276. <https://doi.org/10.1021/acsenvironau.3c00002>
15. Song, H. and Ye, J., *Trends in Chem.*, 2022, vol. 4, no. 12, pp. 1094–11054. <https://doi.org/10.1016/j.trechm.2022.09.003>
16. Li, Q., Ouyang, Y., Li, H., Wang, L., and Zeng, J., *Angew. Chem. Int. Ed.*, 2022, vol. 61, no. 2, Art. ID: e202108069. <https://doi.org/10.1002/anie.202108069>
17. Zhu, Z., Guo, W., Zhang, Y., Pan, Ch., Xu, J., Zhu, Y., and Lou, Y., *Carbon Energy*, 2021, vol. 3, no. 4, pp. 519–540. <https://doi.org/10.1002/cey2.127>
18. Ivanov, R.E., Zharkov, M.N., and Zlotin, S.G., *ChemPhotoChem*, 2022, vol. 6, no. 8, Art. ID: e202200084. <https://doi.org/10.1002/cptc.202200084>
19. Zhou, M., and Wang, H., *J. Am. Chem. Soc. Au*, 2022, vol. 2, no. 1, pp. 188–196. <https://doi.org/10.1021/jacsau.1c00466>
20. Jiang, Y., Fan, Y., Li, S., and Tang, Z., *CCS Chem.*, 2023, vol. 5, pp. 30–54. <https://doi.org/10.31635/ccschem.022.202201991>
21. Jiang, W., Low, B.Q.L., Long, R., Low, J., Loh, H., Tang, K.Y., Chai, C.H.T., Zhu, H., Zhu, H., Li, Z., Loh, X.J., Xiong, Y., and Ye, E., *ACS Nano*, 2023, vol. 17, no. 5, pp. 4193–4229. <https://doi.org/10.1021/acsnano.2c12314>
22. Li, Y., Luo, L., Zhang, J., Hao, G., Jiang, W., and Liu, G., *Next Energy*, 2025, vol. 8, Art. ID: 100274. <https://doi.org/10.1016/j.nxener.2025.100274>
23. Li, H., Li, R., Liu, G., Zhai, M., and Yu, J., *Adv. Mater.*, 2023, Art. ID: 2301307. <https://doi.org/10.1002/adma.202301307>
24. Zhang, Q., Ma, J., Zheng, X., Masakazu, A., Wang, L., and Zhang, J., *Catal. Lett.*, 2023, vol. 153, pp. 2223–2244. <https://doi.org/10.1007/s10562-022-04149-2>
25. Xia, Y., Sayed, M., Zhang, L., Cheng, B., and Yu, J., *Chem. Catal.*, 2021, vol. 1, no. 6, pp. 1173–1214. <https://doi.org/10.1016/j.checat.2021.08.009>
26. Kumar, P., Al-Attas, T.A., Hu, J., and Kibria, M.G., *ACS Nano*, 2022, vol. 16, no. 6, pp. 8557–8618. <https://doi.org/10.1021/acsnano.2c02464>
27. Zhou, P., Luo, M., and Guo, S., *Nat. Rev. Chem.*, 2022, vol. 6, pp. 823–838. <https://doi.org/10.1038/s41570-022-00434-1>
28. Yang, Q., Jiang, Y., Zhuo, H., Mitchell, E.M., and Yu, Q., *Nano Energy*, 2023, vol. 111, Art. ID: 108404. <https://doi.org/10.1016/j.nanoen.2023.108404>
29. Wu, J., Shi, H., Li, K., and Guo, X., *Current Opinion Chem. Eng.*, 2023, vol. 40, Art. ID: 100923. <https://doi.org/10.1016/j.coche.2023.100923>
30. Li, R. and Wang, D., *Nano Res.*, 2022, vol. 15, no. 8, pp. 6888–6923. <https://doi.org/10.1007/s12274-022-4371-x>
31. Shoji, S., Peng, X., Yamaguchi, A., Watanabe, R., Fukuhara, C., Cho, Y., Yamamoto, T., Matsumura, S., Yu, M.W., Ishii, S., Fujita, T., Abe, H., and Miyauchi, M., *Nat. Catal.*, 2020, vol. 3, pp. 148–153. <https://doi.org/10.1038/s41929-019-0419-z>
32. Wang, X., Luo, N., and Wang, F., *Chin. J. Chem.*, 2022, vol. 40, no. 12, pp. 1492–1505. <https://doi.org/10.1002/cjoc.202200028>
33. Xu, Y., Chen, E., and Tang, J., *Carbon Future*, 2023, vol. 12, Art. ID: 9200004. <https://doi.org/10.26599/CF.2023.9200004>
34. Wu, X., Zhang, H., Xie, Sh., and Wang, Y., *Chem. Catal.*, 2023, vol. 3, no. 2, Art. ID: 100437. <https://doi.org/10.1016/j.checat.2022.10.013>

35. Januario, E.R., Silvaino, P.F., Machado, A.P., Vaz, J.M., and Spinace, E.V., *Frontiers in Chemistry*, 2021, vol. 9.  
<https://doi.org/10.3389/fchem.2021.685073>
36. Ma, J., Long, R., Liu, D., Low, J., and Xiong, Y., *Small Structures*, 2022, vol. 3, no. 1, Art. ID: 2100147.  
<https://doi.org/10.1002/sstr.202100147>
37. Chebbi, A., Sinopoli, A., Abotaleb, A., and Bicer, Y., *Catal. Sci. Technol.*, 2023, vol. 13, no. 17, pp. 4895–4918.  
<https://doi.org/10.1039/D3CY00675A>
38. Kozlova, E.A., Lyulyukin, M.N., Kozlov, D.V., and Parmon, V.N., *Russ. Chem. Rev.*, 2021, vol. 90, no. 12, pp. 1520–1543.  
<https://doi.org/10.1070/RCR5004>
39. Hu, Q., Li, Y., Cao, H., Ji, L., Wu, J., and Zhong, M., *J. Colloid Interface Sci.*, 2024, vol. 657, pp. 942–952.  
<https://doi.org/10.1016/j.jcis.2023.12.032>
40. Chen, Y., Cao, H., Li, Y., Hu, Q., Wu, J., and Zhang, Zh., *Solar RRL*, 2023, vol. 7, no. 12, Art. ID: 2300216.  
<https://doi.org/10.1002/solr.202300216>
41. Pan, F., Xiang, X., Deng, W., Zhao, H., Feng, X., and Li, Y., *ChemCatChem*, 2018, vol. 10, no. 5, pp. 940–945.  
<https://doi.org/10.1002/cctc.201701565>
42. Pan, F., Xiang, X., Du, Z., Sarnello, E., Li, T., and Li, Y., *Appl. Catal. B: Environ.*, 2020, vol. 260, Art. ID: 118189.  
<https://doi.org/10.1016/j.apcatb.2019.118189>
43. Cao, H., Li, Y., Hu, Q., Wu, J., Zhong, M., and Ji, L., *Chem. Eng. J.*, 2024, vol. 481, Art. ID: 148551.  
<https://doi.org/10.1016/j.cej.2024.148551>
44. Cao, H., Li, Y., Hu, Q., Wu, J., and Ji, L., *J. Mater. Chem. A*, 2023, vol. 11, pp. 19645–19655.  
<https://doi.org/10.1039/D3TA04267G>
45. Zhou, L., Martirez, J.M.P., Finzel, J., Zhang, C., Swearer, D.F., Tian, S., Robotjazi, H., Lou, M., Dong, L., Henderson, L., Christopher, Ph., Carter, E.A., Nordlander, P., and Halas, N.J., *Nat. Energy*, 2020, vol. 5, no. 1, pp. 61–70.  
<https://doi.org/10.1038/s41560-019-0517-9>
46. Cho, Y., Shoji, S., Yamaguchi, A., Hoshina, T., Fujita, T., Abe, H., and Miyauchi, M., *Chem. Commun.*, 2020, vol. 56, no. 33, pp. 4611–4614.  
<https://doi.org/10.1039/D0CC00729C>
47. Gao, Ch., Low, J., Long, R., Kong, T., Zhu, J., and Xiong, Y., *Chem. Rev.*, 2020, vol. 120, pp. 12175–12216.  
<https://doi.org/10.1021/acs.chemrev.9b00840>
48. Li, Zh., Yi, Zh., Li, Zh., and Zou, Zh., *Solar RRL*, 2021, vol. 5, no. 6, Art. ID: 2000596.  
<https://doi.org/10.1002/solr.202000596>
49. Wang, T., Tian, B., Han, B., Ma, D., Sun, M., Hanif, A., Hia, D., and Shang, J., *Energy Environ. Mater.*, 2022, vol. 5, no. 33, pp. 711–730.  
<https://doi.org/10.1002/eem2.12229>
50. Cheng, X.M., Zhao, J., and Sun, W.Y., *Energy-Chem*, 2022, vol. 4, no. 5, Art. ID: 100084.  
<https://doi.org/10.1016/j.enchem.2022.100084>
51. Sun, X., Zhang, X., and Xie, Y., *Matter*, 2020, vol. 2, no. 4, pp. 842–861.  
<https://doi.org/10.1016/j.matt.2020.02.006>
52. Ma, Z., Chen, Y., Gao, Ch., and Xiong, Y., *Energy & Fuels*, 2022, vol. 36, no. 19, pp. 11428–11442.  
<https://doi.org/10.1021/acs.energyfuels.2c01351>
53. Zhang, C., Wang, J., Ouyang, S., Song, H., Ye, J., and Shi, L., *Sci. China Chem.*, 2023, vol. 66, no. 9, pp. 2532–2557.  
<https://doi.org/10.1007/s11426-023-1737-2>
54. Khlebtsov, N.G., Dykman, L.A., and Khlebtsov, B.N., *Russ. Chem. Rev.*, 2022, vol. 91, no. 10, Art. ID: RCR5058.  
<https://doi.org/10.57634/RCR5058>
55. Lang, J., Ma, Y., Wu, X., Jiang, Y., and Hu, Y.H., *Green Chem.*, 2020, vol. 22, no. 14, pp. 4669–4675.  
<https://doi.org/10.1039/D0GC01608J>
56. Wang, Ch., Li, X., Ren, Y., Jiao, H., Wang, F.R., and Tang, J., *ACS Catal.*, 2023, vol. 13, no. 6, pp. 3768–3774.  
<https://doi.org/10.1021/acscatal.2c06093>
57. Du, X., Liu, Q., Wang, Zh., Cheng, M., Hu, J., Wei, T., Wang, R., Ling, Y., Li, W., and Liu, B., *Inorg. Chim. Acta*, 2023, vol. 553, Art. ID: 121517.  
<https://doi.org/10.1016/j.ica.2023.121517>
58. Luo, Sh., Ren, X., Lin, H., Song, H., and Ye, J., *Chem. Sci.*, 2021, vol. 12, no. 16, pp. 5701–5719.  
<https://doi.org/10.1039/D1SC00064K>
59. Jiang, H., Peng, X., Yamaguchi, A., Fujita, T., Abe, H., and Miyauchi, M., *Chem. Commun.*, 2019, vol. 55, no. 91, pp. 13765–13768.  
<https://doi.org/10.1039/C9CC06170C>

60. Lv, S., Du, Y., Wu, F., Cai, Y., and Zhou, T., *Nanoscale Adv.*, 2022, vol. 4, no. 12, pp. 2608–2631.  
<https://doi.org/10.1039/D2NA00140C>
61. Mateo, D., Cerrillo, J.L., Durini, S., Gascon, J., *Chem. Soc. Rev.*, 2021, vol. 50, no. 3, pp. 2173–2210.  
<https://doi.org/10.1039/D0CS00357C>
62. Li, M., Sun, Zh., Hu, Y.H., *Chem. Eng. J.*, 2022, vol. 428, Art. ID: 131222.  
<https://doi.org/10.1016/j.cej.2021.131222>
63. Ji, G., Wu, Sh., Song, X., Meng, L., Jia, Y., Tian, J., *Int. J. Hydrogen Energy*, 2024, vol. 57, pp. 696–708.  
<https://doi.org/10.1016/j.ijhydene.2024.01.105>
64. Wu, Sh., Li, Y., Hu, Q., Wu, J., Zhang, Q., *ACS Sustainable Chem. Eng.*, 2021, vol. 9, no. 35, pp. 11635–11651.  
<https://doi.org/10.1021/acssuschemeng.1c03692>
65. Tavasoil, A.V., Preston, M., Ozin, G., *Energy Environ. Sci.*, 2021, vol. 14, no. 5, pp. 3098–3109.  
<https://doi.org/10.1039/D0EE02809F>
66. Feng, X. and Li, Y., in *Nanostructured Materials for Sustainable Energy: Design, Evaluation, and Applications*, Chapter 8, ACS Symposium Series, 2022, vol. 1421, pp. 207–232.  
<https://doi.org/10.1021/bk-2022-1421.ch008>
67. Gao, P., Wang, P., Liu, X., Cui, Z., Wu, Y., Zhang, X., Zhang, Q., Wang, Z., Zheng, Zh., Cheng, H., Liu, Y., Dai, Y., Huang, B., *Catal. Sci. Technol.*, 2022, vol. 12, no. 5, pp. 1628–1636.  
<https://doi.org/10.1039/D1CY02281D>
68. Du, Z., Petru, C., Yang, X., Chen, F., Fang, S., Pan, F., Gang, Y., Zhou, H.C., Hu, Y.H., Li, Y., *J. CO<sub>2</sub> Utilization*, 2023, vol. 67, Art. ID: 102317.  
<https://doi.org/10.1016/j.jcou.2022.102317>
69. Cheng, J., Liu, X., Li, T., Li, D., Jiang, Zh., Xu, D., Patel, B., Guo, Y., *Int. J. Hydrogen Energy*, 2024, vol. 53, pp. 1433–1444.  
<https://doi.org/10.1016/j.ijhydene.2023.12.117>
70. Li, T., Cheng, J., Li, D., Xu, D., Patel, B., Guo, Y., *Int. J. Hydrogen Energy*, 2024, vol. 67, pp. 1194–1205.  
<https://doi.org/10.1016/j.ijhydene.2024.01.004>
71. Yan, X., Lu, B., Dong, H., Liu, Q., *Appl. Energy*, 2023, vol. 348, Art. ID: 121549.  
<https://doi.org/10.1016/j.apenergy.2023.121549>
72. Lorber, K., Zavasnik, J., Sancho-Parramon, J., Bubas, M., Mazaj, M., Djinic, P., *Appl. Catal. B: Environ.*, 2022, vol. 301, Art. ID: 120745.  
<https://doi.org/10.1016/j.apcatb.2021.120745>
73. Tavasoli, A., Gouda, A., Zähringer, T., Li, Y.F., Quaid, F., Perez, C.J.V., Song, R., Sain, M., Ozin, G., *Nat. Commun.*, 2023, vol. 14, Art. ID: 1435.  
<https://doi.org/10.1038/s41467-023-37493-x>
74. Takami, D., Ito, Y., Kawaharasaki, S., Yamamoto, A., Yoshida, H., *Sust. Energy Fuels*, 2019, vol. 3, no. 11, pp. 2968–2971.  
<https://doi.org/10.1039/C9SE00206E>
75. Zhang, G., Liu, J., Xu, Y., Sun, Y., *Int. J. Hydrogen Energy*, 2018, vol. 43, no. 32, pp. 15030–15054.  
<https://doi.org/10.1016/j.ijhydene.2018.06.091>
76. Al-Fatesh, A.S., El-Salamony, R.A., Roushdy, M.H., Alwan, S.M., Osman, A.I., Alfatesh, S.A., Ahmed, H., Fakeeha, A.H., Ibrahim, A.A., *Adv. Mater.*, 2024, vol. 11, no. 1, Art. ID: 2300509.  
<https://doi.org/10.1002/admi.202300509>
77. Ul Hasnain, S.M.W., Farooqi, A.S., Ayodele, B.V., Farooqi, A.S., Sanallah, Kh., Abdullah, B., *J. Cleaner Production*, 2024, vol. 434, Art. ID: 139904.  
<https://doi.org/10.1016/j.jclepro.2023.139904>
78. Loktev, A.S., Arkhipova, V.A., Bykov, M.A., Sadovnikov, A.A., Dedov, A.G., *Petr. Chem.*, 2023, vol. 63, no. 4, pp. 607–617.  
<https://doi.org/10.1134/s0965544123040023>
79. Androulakis, A., Yentekakis, I.V., Panagiotopoulos, P., *Int. J. Hydrogen Energy*, 2023, vol. 48, no. 87, pp. 33886–33902.  
<https://doi.org/10.1016/j.ijhydene.2023.03.114>
80. Zhou, W., Wang, B.H., Tang, L., Chen, L., Guo, J.K., Pan, J.B., Lei, B., Hu, B., Bai, Zh.J., Tulu, M., Li, Z.X., Wang, X., Au, Ch.T., Yin, Sh.F., *Adv. Funct. Mater.*, 2023, vol. 33, no. 27, Art. ID: 2214068.  
<https://doi.org/10.1002/adfm.202214068>
81. Takami, D., Yamamoto, A., and Yoshida, H., *Catal. Sci. Technol.*, 2020, vol. 10, no. 17, pp. 5811–5814.  
<https://doi.org/10.1039/D0CY00858C>
82. Takami, D., Yamamoto, A., Kato, K., Shishido, T., and Yoshida, H., *J. Phys. Chem. C*, 2022, vol. 126, no. 37, pp. 15736–15743.  
<https://doi.org/10.1021/acs.jpcc.2c05291>
83. Zhang, J., Li, Y., Sun, J., Chen, H., Zhu, Y., Zhao, X., Zhang, L.Ch., Wang, Sh., Zhang, H., Duan, X., Shi, L., Zhang, Sh., Zhang, P., Shao, G., Wu, M., Wang, Sh., and Sun, H., *Appl. Catal. B: Environ.*, 2022, vol. 309, Art. ID: 121263.  
<https://doi.org/10.1016/j.apcatb.2022.121263>

84. Zhang, Zh.Y., Li, T., Yao, J.L., Xie, T., and Xia, Q., *Molecular Catal.*, 2023, vol. 535, Art. ID: 112828. <https://doi.org/10.1016/j.mcat.2022.112828>
85. Zhang, Zh.Y., Zhang, T., Liang, W.P., Bai, P.W., Zheng, H.Y., Lei, Y., Hu, Zh., and Xie, T., *Energ. Convers. Manag.*, 2022, vol. 258, Art. ID: 115496. <https://doi.org/10.1016/j.enconman.2022.115496>
86. Zhu, Z., Tang, R., Li, C., An, X., and He, L., *Adv. Sci.*, 2023, vol. 10, no. 24, Art. ID: e2302568. <https://doi.org/10.1002/advs.202302568>
87. Karakaya, C., and Kee, R.J., *Prog. Energy Combust.*, 2016, vol. 55, pp. 60–97. <https://doi.org/10.1016/j.pecs.2016.04.003>
88. Wang, P., Shi, R., Zhao, J., and Zhang, T., *Adv. Sci.*, 2024, vol. 11, no. 8, Art. ID: 2305471. <https://doi.org/10.1002/advs.202305471>
89. Meng, L., Chen, Z., Ma, Z., He, S., Hou, Y., Li, H., Yuan, R., Huang, X., Wang, X., and Wang, Long, J., *Energy Environ. Sci.*, 2018, vol. 11, pp. 294–298. <https://doi.org/10.1039/C7EE02951A>
90. Amano, F., Akamoto, C., Ishimaru, M., Inagaki, S., and Yoshida, H., *Chem. Commun.*, 2020, vol. 56, pp. 6348–6351. <https://doi.org/10.1039/D0CC01730B>
91. Li, L., Li, G.D., Yan, C., Mu, X.Y., Pan, X.L., Zou, X.X., Wang, K.X., and Chen, J.Sh., *Angew. Chem. Int. Ed.*, 2011, vol. 50, no. 36, pp. 8299–8303. <https://doi.org/10.1002/anie.201102320>
92. Li, L., Cai, Y., Li, G., Mu, X., Wang, K., and Chen, J., *Angew. Chem. Int. Ed.*, 2012, vol. 51, no. 19, pp. 4702–4706. <https://doi.org/10.1002/anie.201200045>
93. Yu, L., and Li, D., *Catal. Sci. Technol.*, 2017, vol. 7, pp. 635–640. <https://doi.org/10.1039/C6CY02435A>
94. Yu, L., Shao, Y., and Li, D., *Appl. Catal. B: Env.*, 2017, vol. 204, pp. 216–223. <https://doi.org/10.1016/j.apcatb.2016.11.039>
95. Yu, X., Zholobenko, V.L., Moldovan, S., Hu, D., Wu, D., Ordonsky, V., and Khodakov, A., *Nat. Energy*, 2020, vol. 5, no. 7, pp. 511–519. <https://doi.org/10.1038/s41560-020-0616-7>
96. Singh, S.P., Anzai, A., Kawaharasaki, S., Yamamoto, A., and Yoshida, H., *Catal. Today*, 2021, vol. 375, pp. 264–272. <https://doi.org/10.1016/j.cattod.2020.04.023>
97. Singh, S.P., Yamamoto, A., Fudo, E., Tanaka, A., Kominami, H., and Yoshida, H., *ACS Catal.*, 2021, vol. 11, no. 22, pp. 13768–13781. <https://doi.org/10.1021/acscatal.1c03786>
98. Liu, Y., Chen, Y., Jiang, W., Kong, T., Camargo, P.H.C., and Gao, Ch., Xiong, Y., *Research*, 2022, vol. 19, pp. 1–12. <https://doi.org/10.34133/2022/9831340>
99. Zhang, H., Zhong, W., Gong, Q., Sun, P., Fei, X., Wu, X., Xu, Sh., Zhang, Q., Fu, G., Xie, Sh., and Wang, Y., *Angew. Chem. Int. Ed.*, 2023, vol. 62, no. 25, Art. ID: e202303405. <https://doi.org/10.1002/anie.202303405>
100. Shen, T., Wang, Z., Xu, S.M., Sun, X., Liu, G., Bai, S., Li, J., Song, Z., Zheng, L., and Song, Y.F., *Cell Reports Phys. Sci.*, 2023, vol. 4, no. 7, Art. ID: 101478. <https://doi.org/10.1016/j.xcrp.2023.101478>
101. Machado, A.P., Carminati, S.A., Januário, E.R., Ferreira, P.S., Vaz, J.M., and Spinacé, E.V., *Methane*, 2023, vol. 2, no. 1, pp. 44–55. <https://doi.org/10.3390/methane2010003>
102. Ishimaru, M., Amano, F., Akamoto, Ch., and Yamazoe, S., *J. Catal.*, 2021, vol. 397, pp. 192–200. <https://doi.org/10.1016/j.jcat.2021.03.024>
103. Amano, F., Ishikawa, A., Sato, H., Akamoto, Ch., Singh, S.P., Yamazoe, S., and Sugimoto, T., *Catal. Today*, 2024, Art. ID: 114375. <https://doi.org/10.1016/j.cattod.2023.114375>
104. Zhang, J., Shen, J., Li, D., Long, J., Gao, X., Feng, W., Zhang, Sh., Zhang, Z., Wang, X., and Yang, W., *ACS Catal.*, 2023, vol. 13, no. 3, pp. 2094–2105. <https://doi.org/10.1021/acscatal.2c05081>
105. Chen, Z.A., Yan, X., and Zhi, M., *Colloid Surf.: Physicochem. Eng. Aspects*, 2024, vol. 680, Art. ID: 132712. <https://doi.org/10.1016/j.colsurfa.2023.132712>
106. Ma, J., Low, J., Wu, D., Gong, W., Liu, H., Liu, D., Long, R., and Xiong, Y., *Nanoscale Horiz.*, 2022, vol. 8, no. 1, pp. 63–68. <https://doi.org/10.1039/D2NH00457G>
107. Tang, H., Chen, Z.A., Ouyang, Ch., Ye, Z., Li, Sh., Hong, Zh., and Zhi, M., *J. Phys. Chem. C*, 2022, vol. 126, no. 47, pp. 20036–20048. <https://doi.org/10.1021/acs.jpcc.2c06373>
108. Wu, S., Tan, X., Lei, J., Chen, H., Wang, L., and Zhang, J., *J. Am. Chem. Soc.*, 2019, vol. 141, no. 16, pp. 6592–6600. <https://doi.org/10.1021/jacs.8b13858>

109. Wang, J., Peng, Y., and Xiao, W., *Sci. China Chem.*, 2023, vol. 66, no. 11, pp. 3252–3261. <https://doi.org/10.1007/s11426-023-1766-8>
110. Chen, Z., Wu, Sh., Ma, J., Mine, Sh., Toyao, T., Matsuo, M., Wang, L., and Zhang, J., *Angew. Chem. Int. Ed.*, 2021, vol. 60, no. 21, pp. 11901–11909. <https://doi.org/10.1002/anie.202016420>
111. Feng, X., Kang, K., Wu, Y., Zhang, J., and Wang, L., *Chem. Commun.*, 2021, vol. 57, no. 96, pp. 13000–13003. <https://doi.org/10.1039/D1CC04663B>
112. Zhang, W., Fu, C., Low, J., Duan, D., Ma, J., Jiang, W., Chen, Y., Liu, H., Qi, Z., Long, R., Yao, Y., Li, X., Zhang, H., Liu, Zh., Yang, J., Zou, Zh., and Xiong, Y., *Nat. Commun.*, 2022, vol. 13, no. 1, Art. ID: 2806. <https://doi.org/10.1038/s41467-022-30532-z>
113. Xiao, M., Wang, L., Wang, H., Yuan, J., Chen, X., Zhang, Z., Fu, X., and Dai, W., *Catal. Sci. Technol.*, 2023, vol. 13, no. 14, pp. 4148–4155. <https://doi.org/10.1039/D3CY00515A>
114. Tang, Ch., Du, Sh., Huang, H., Tan, S., Zhao, J., Zhang, H., Ni, W., Yue, X., Ding, Zh., Zhang, Z., Yuan, R., Dai, W., Fu, X., Roeffaers, M.B.J., and Long, J., *ACS Catal.*, 2023, vol. 13, no. 10, pp. 6683–6689. <https://doi.org/10.1021/acscatal.3c00507>
115. Jiang, W., Low, J., Mao, K., Duan, D., Chen, Sh., Liu, W., Pao, Ch., Ma, J., Sang, Sh., Shu, Ch., Zhan, X., Qi, Z., Zhang, H., Liu, Zh., Wu, X., Long, R., Song, L., and Xiong, Y., *J. Am. Chem. Soc.*, 2021, vol. 143, no. 1, pp. 269–278. <https://doi.org/10.1021/jacs.0c10369>
116. Wu, M., Tang, H., Ye, Z., Li, S., and Zhi, M., *Energy Fuels*, 2023, vol. 37, no. 14, pp. 10603–10614. <https://doi.org/10.1021/acs.energyfuels.3c00834>
117. Zheng, K., Zhang, X., Hu, J., Xu, Ch., Zhu, J., Li, J., Wu, M., Zhu, Sh., Li, L., Wang, Sh., Lv, Y., He, X., Zuo, M., Liu, Ch., Pan, Y., Zhu, J., Sun, Y., and Xie, Y., *Sci. China Chem.*, 2024, vol. 67, no. 3, pp. 869–875. <https://doi.org/10.1007/s11426-023-1792-8>
118. Wang, J., Tafen, De N., Lewis, J.P., Hong, Zh., Manivanan, A., Zhi, M., Li, M., and Wu, N., *J. Am. Chem. Soc.*, 2009, vol. 131, no. 34, pp. 12290–12297. <https://doi.org/10.1021/ja903781h>
119. Hu, D., Ordonsky, V.V., and Khodakov, A.Y., *Appl. Catal. B: Environ.*, 2021, vol. 286, Art. ID: 119913. <https://doi.org/10.1016/j.apcatb.2021.119913>
120. Kwon, Y., Kim, T., Kwon, G., Yi, J., and Lee, H., *J. Am. Chem. Soc.*, 2017, vol. 139, no. 48, pp. 17694–17699. <https://doi.org/10.1021/jacs.7b11010>
121. Sato, H., Ishikawa, A., Saito, H., Higashi, T., Takeyasu, K., and Sugimoto, T., *Commun. Chem.*, 2023, vol. 6, Art. ID: 8. <https://doi.org/10.1038/s42004-022-00803-3>
122. Sinev, M.Y., *Kinet. Catal.*, 2019, vol. 60, no. 4, pp. 420–431. <https://doi.org/10.1134/S0023158419040177>
123. Xiao, Y. and Varma, A., *ACS Catal.*, 2018, vol. 8, pp. 2735–2740. <https://doi.org/10.1021/acscatal.8b00156>
124. Dutta, K., Shahryari, M., and Kopyscinski, J., *Ind. Eng. Chem. Res.*, 2020, vol. 59, no. 10, pp. 4245–4256. <https://doi.org/10.1021/acs.iecr.9b05548>
125. Chen, Z., Ye, Y., Feng, X., Wang, Y., Han, X., Zhu, Y., Wu, Sh., Wang, S., Yang, W., Wang, L., and Zhang, J., *Nat. Commun.*, 2023, vol. 14, Art. ID: 2000. <https://doi.org/10.1038/s41467-023-37663-x>
126. Ma, J., Zhang, Q., Chen, Z., Kang, K., Pan, L., Wu, Sh., Chen, Ch., Wu, Zh., Zhang, J., and Wang, L., *Chem. Catal.*, 2023, vol. 2, no. 7, pp. 1775–1792. <https://doi.org/10.1016/j.checat.2022.05.016>

**Publisher's Note.** Pleiades Publishing remains neutral with regard to jurisdictional claims in published maps and institutional affiliations.

AI tools may have been used in the translation or editing of this article.